2011

Enhancing Cnt-composites With Raman Spectroscopy

Gregory J. Freihofer
University of Central Florida

ENHANCING CNT-COMPOSITES WITH RAMAN SPECTROSCOPY

by

Gregory J. Freihofer
B.S. University of Central Florida, 2010

A thesis submitted in partial fulfillment of the requirements
for the degree of Master of Science
in the Department of Mechanical, Materials and Aerospace Engineering
in the College of Engineering and Computer Science
at the University of Central Florida
Orlando, Florida

Fall Term
2011

Major Professor:
Seetha Raghavan

Abstract

Carbon Nanotubes (CNTs) have been the subject of intense research for their potential to improve a variety of material properties when developed as nano-composites. This research aims to address the challenges that limit the ability to transfer the outstanding nano-scale properties of CNTs to bulk nano-composites through Raman characterization. These studies relate the vibrational modes to microstructural characterization of CNT composites including stress, interface behavior, and defects. The formulation of a new fitting procedure using the pseudo-Voigt function is presented and shown to minimize the uncertainty of characteristics within the Raman G and D doublet. Methods for optimization of manufacturing processes using the Raman characterization are presented for selected applications in a polymer multiwalled nanotube (MWNT) composite and laser-sintered ceramic-MWNT composite. In the first application, the evolution of the MWNT microstructure throughout a functionalization and processing of the polymer-MWNT composite was monitored using the G peak position and D/G intensity ratio. Processing parameters for laser sintering of the ceramic-MWNT composites were optimized by obtaining maximum downshift in stress sensitive G-band peak position, while keeping disorder sensitive D/G integrated intensity ratio to a minimum. Advanced Raman techniques, utilizing multiple wavelengths, were used to show that higher excitation energies are less sensitive to double resonance Raman effects. This reduces their influence and allows the microstructural strain in CNT composites to be probed more accurately.

The use of these techniques could be applied to optimize any processing parameters in the manufacturing of CNT composites to achieve enhanced properties.

I would like to dedicate this work to my family, who supported me in all of my academic endeavors

Acknowledgments

My work could not have been possible without the help and support from all of my family. I would like to give special thanks to my sisters Cathy and Amy, who gave me inspiration into and helping make the world a better place and the value of family. I would like to thank my brother Eddie, who assisted me in my programing challenges. I would like to thank my Cousin Brent, who taught me to take advantage of my situation. Especially give thanks to my mother and father who always supported me through my research. I also like to acknowledge all my friends and colleagues in academia who helped me refine my ideas. I would like to thank my advisor Dr. Raghavan for giving me a vision into the future of CNTs, materials, and their technology. I would like to thank the scientist at the Argonne Nation Labs who helped train and assist me in the field of nano-science. Use of the Center for Nanoscale Materials was supported by the U. S. Department of Energy, Office of Science, Office of Basic Energy Sciences, under Contract No. DE-AC02-06CH11357. Dr. Gou Jihua (UCF) is acknowledged for providing the CNT samples for our experiments and the images of the samples. The genetic algorithm codes used in our spectral analysis programs were courtesy of Dr William Crossley (Purdue University).

TABLE OF CONTENTS

LIST OF FIGURES

LIST OF TABLES

CHAPTER 1
INTRODUCTION

1.1 Motivation and Background

Carbon nanotubes (CNTs) have received much attention since their discovery by Iijima [37], and are one of the most likely candidates for future nano-composites [103]. They have a number of unique properties including, super strength to weight ratio [88], excellent electrical and thermal conductivities [5], and optical properties [45]. Their exceptional properties have great potential in future applications, and they have even been proposed to be used in designing elevators into space [75], and large suspended bridges [13]. However, there are many challenges that limit CNTs from being implemented in conventional applications which reflect their nanoscale properties. Research in such areas as dispersion of the CNTs [61], alignment [109], and good interface properties [57] will pave the way for progress in exploiting their excellent properties. Development of a characterization techniques to study and monitor the latter properties is integral to achieve success in the manufacturing and testing of composites. The goal of this study was to present novel methods in enhancing CNT composites with correlating their microstructural properties with Raman spectroscopy. Optimization techniques for a wide range of different manufacturing processes was discovered to be possible.

Raman spectroscopy has been the primary experimental means to validate physical phenomenon of CNTs with several review papers published on well established Raman

theory [12, 21, 22, 41, 20, 40]. The Raman spectra probes vibrational domains at the atomic scale, and has been correlated with many characteristics, acting as a tool to monitor the structural purity [67, 68], and functionalizations [89, 64, 78] of a CNT's structure, dispersion of CNTs [87], interface properties with matrix [32, 105, 33], and alignment [114]. There are many processes involved with purifying, functionalizing, and processing CNTs into composites [54, 31], all of which have the potential to be fully optimized with Raman spectroscopy. In this study, many stress sensing and disorder sensitive Raman properties are used to discover the effectiveness of various manufacturing process parameters. Methods to enhance CNT-composite properties through Raman characterization, a non-invasive measurement technique, are investigated. These methods have the potential to be introduced in the optimization of future pilot manufacturing assembly lines for novel CNT composites.

1.2 Physical structure of CNTs

It is first necessary to understand the physical structure of CNTs before discussing, in detail, the physical interpretation of their Raman spectra. Many review papers discussing the quasi 1-D optical phenomenon of CNTs usually begin by first explaining their basic physical structure of single walled nanotubes (SWNTs) [12, 21, 22]. Here, multi-walled carbon nanotubes (MWNTs) were used in the experimental studies presented in later

chapters. However, MWNT's constituent SWNT structure will be briefly identified to compare some overlapping physical characteristics.

All physical properties of a SWNT can be derived from their (n,m) indices's including metallic or semi-conducting character, diameter, and chirality [12]. Each combination of (n,m) will produce a "species" of carbon nanotubes. Burghard showed these (n,m) indices can yield diameter and chirality of the CNT in equation 1.1 and 1.2 respectively [12]. Evidence from recent studies suggests that the chiral angle has a large role to play in dictating the physical properties of CNTs [53].

SWNTs have unique optical transitions, created by a strong coupling that occurs between the electrons and phonons in the quasi 1-D structure [21]. These unique optical properties allow the SWNTs to be specifically identified with respect to their (n,m) indices [42]. This identification process would be more challenging for MWNTs, because such a large density of n,m combinations are possible for a given diameter.

$$d_t = \frac{a}{\pi}\sqrt{(n^2 + nm + m^2)} \tag{1.1}$$

$$\theta = tan^{-1}(\frac{\sqrt{3}m}{m + 2n}) \tag{1.2}$$

1.3 The Raman spectrum for MWNTs

This section will discuss most features in the Raman spectrum, with a primary focus on the G and D doublet. The G and D doublet was the focus of the experimental work throughout this study because of the possibility to derive disorder [4, 68, 40] and microstructural strain [48, 60] within a relatively narrow frequency range. Phenomenon associated with the G' and other higher energy vibrations will be discussed, as they are sometimes referred to be more sensitive [63] or have the ability to probe additional information [4] than the lower energy features within the G and D doublet.

1.3.1 The G and D doublet for MWNTs

The G and D doublet is a commonly used Raman phenomenon to characterize CNTs [40] and various types of carbon structures [25, 24]. G band peak position is dependent on environmental effects, such as hydrostatic [60, 108] and uniaxial [16, 28, 49] stress, temperature [81, 52, 34, 121, 59, 104], and electronic charge [78, 65, 118]. The origin of the G band will be discussed, along with its neighboring sub-bands and their potential applications.

Because of a strong Raman resonance enhancement, the G bands of SWNTs behave differently from other forms of carbon. For SWNTs, the G band has been accepted to encompass 6 Raman modes of A, E_1 and E_2 symmetry [72], for which the relative

intensities are sensitive to the chiral angle [43, 108, 74, 79]. When CNTs contain an increasing number of concentric walls, the G band begins to broaden and consolidate into a single peak from a super-positioning of constituting tubes [119]. Hence, the Raman spectra for MWNTs is far less straight forward, as it closely resembles that of graphite and other carbonaceous structures [6]. Fig. 1.1 illustrates a comparison between the G and D doublet for MWNT and SWNT. The enhanced D-band for MWNTs has been associated with the increased possibility of disorder within the concentric walls of MWNTs[69].

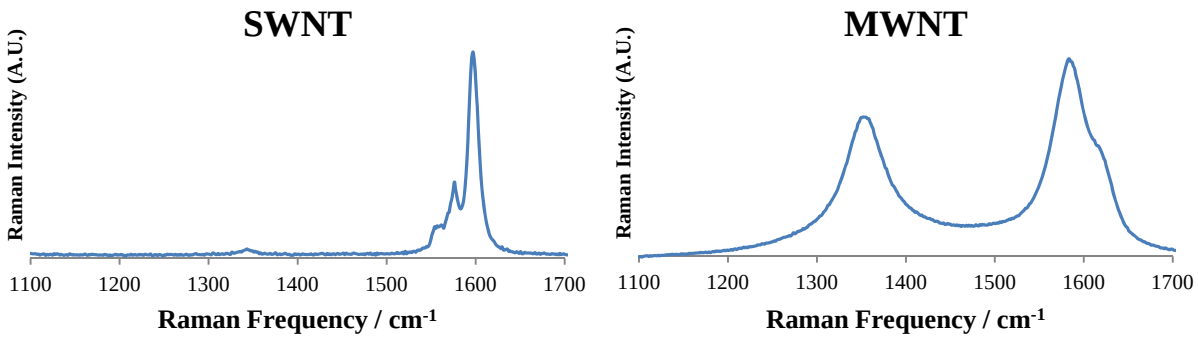

Figure 1.1: Here a comparison between the G and D doublet for MWNT and SWNT is made. The several sub-bands that are observable for the SWNT is an enhancement of the Raman resonance for SWNT as compared to the MWNT. Both samples were measured with a 514.4 nm excitation wavelength.

Typically, the three main features that are within the G and D doublet for MWNTs, are the D band ($1365cm^{-1}$), G band ($1580cm^{-1}$), and D' band ($1610cm^{-1}$) [68, 2, 93, 48]. The G-band is an in-plane, tangential, C-C stretching mode assigned to E_{2g} symme-

try [68]. The D band is a disorder induced phonon that could originate from various types of defects and grain boundaries [9]; a product of a double resonance Raman process [101, 86, 85]. The D band's intensity has been experimentally observed to increase with decreasing micro-crystallite size for most carbon materials [110, 23, 46]. The D' band is relatively small for visible excitations, and appears as a subtle bulge on the upper frequency side of G. This band has also been also attributed to a double resonance process [101, 85], but more specifically, it has been used to characterize intercalation between graphitic walls [68] and covalent bonding on the surface of the CNTs [15].

Additional sub-bands were also adapted from similar Raman profiles of industrial soot [83] and wood [115, 123]. Even though these profiles were not from MWNT samples, they still contained the G and D doublet shape that is intrinsic to carbon structures, and offered alternative fitting procedures. Including the G, D, and D' bands, these studies utilized up to six line-shape functions by incorporating a T band ($1120cm^{-1}$), I band ($1250m^{-1}$), and A band ($1500cm^{-1}$). The T band, with relatively low intensity, has be en attributed to sp^3 carbons [24, 115] and appears as a shoulder on the lower frequency side of D in our Raman profile in Fig. 1.2. The I band has been attributed to impurity ions [115], or C=C and C-C stretching modes of polyene-like structures [83]. The A band has been attributed to amorphous carbon [83]. This work presents the first known effort to determine the benefits of adding additional peaks to the G and D doublet of MWNTs.

The most important of the latter characteristics within the G and D doublet are the G band peak position and the D/G ratio. Additional characteristics may exist within the

G and D doublet, and future work should intend to establish the relationships. However, the G band position and the D/G ratio are the characteristics used the most through this study and in literature.

1.3.2 G' and other MWNT Raman features

There are many other features in the Raman spectrum for MWNTs. Presented in Figure 1.2, is a typical extended scan of a MWNT sample covering a relatively wide frequency range. Many high order features are observed, such as the second order bands (G', D+G, 2D'), and even a third order band, 2D+G, was observed at $\approx 4300 cm^{-1}$. Sixth order bands have been observed in graphite whiskers, whose appearance was attributed to a high symmetrical structure [97]. This section attempts to identify these additional higher order features in Fig. 1.2, and discuss differences with the first order spectra.

Most features have been convincingly identified as intrinsic bands to carbon structures [23, 46]. The band under recent investigation has been the band at $\approx 2450\ cm^{-1}$. In a study by Shimada *et al.*, it was assigned as an overtone of an longitudinal (LO) phonon [92]. The second order spectra for SWNTs is much more intricate with several additional bands coming into resonance that are not commonly visible in MWNT's Raman spectra [8, 10]. The focus of this study will remain on the MWNT Raman spectrum, and the SWNT bands were not investigated here.

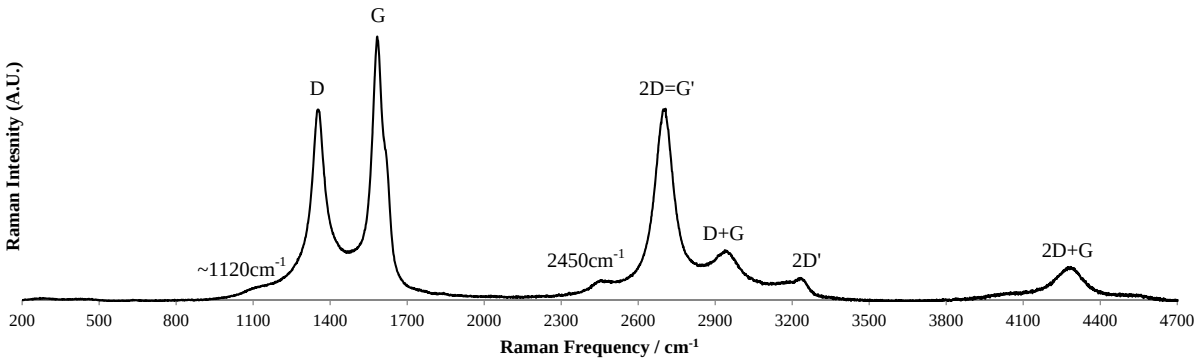

Figure 1.2: An extended scan of a MWNT thin film

A first order Raman feature, such as the G and D doublet, is very sensitive to defects in the carbon sheets, whereas the second order spectra is very sensitive to staking disorder along the crystallographic x-axis [4]. Baldan *et al*. showed that an intensity ratio of the second order spectra, (D+G)/2D, was inversely related to the enhanced ordering of a lamellar structure for reticulated vitreous carbon [4].

Surprisingly little work has been done correlating these second order features to MWNT properties [2], despite evidence of their correlation with disorder of staked graphene sheets. The G' band generally more sensitive to environmental affects such as stress [16], temperature [120], and effects of disorder [63]. The G and D doublet was the focus of this report, because a comprehensive understanding of the fundamental region is necessary to understand second and third order overtones and combinations. However, the G' band was seen to be more sensitive to laser sintering affects studied in this work, and will be presented in the results.

1.4 Raman with variable excitation wavelength

Raman spectroscopy for MWNTs is most commonly used as just a single excitation wavelength usually in the visible spectrum. Most reviews do not even mention the characterization techniques possible with using multiple wavelength excitations [50, 6] when comparing different optical characterization techniques such as Photoluminescence [53, 3] or Rayleigh scattering [91] for CNTs. This is partly due to the fairly new field and complex characterization methods of multiple wavelength spectroscopy. This section briefly describes how multiple wavelength spectroscopy can benefit characterization techniques for CNT and their composites.

Some Raman characteristics are sensitive to laser excitation energy and shift with tuning of laser wavelength. This shifting is henceforth called "dispersion", and such Raman features such as the D and G' peak position disperse at various rates, with sensitivity depending on the microstructure [97]. This dispersion is well documented, and physicists explain it is as a result of a double resonance process (DRR) [71]. Recently, studies have identified that the dispersions have relationships with disorder and this was used to optimize an oxidation process [48]. However, much work is required to understand the differences in the dispersion between SWNTs [80], MWNTs [48], and disorder carbons [24] because they all exhibit distinguishable characteristics.

For SWNTs, the number of discrete geometries available for diameters smaller than 3 nm, open up optical transitions throughout the visible excitation range [27]. This allows

for a resonance Raman process that allows for a selection of SWNTs in resonance with specific excitation energies that match their optical transitions [99, 42, 19]. As the geometries become more continuous with large diameter, the CNT's optical transitions are not experimentally observed, and little work has been done to calculate them. Thus larger diameter CNTs, such as MWNTs, behave more like disordered carbon or graphite [25, 24] rather than SWNTs.

For disordered carbons, and graphite, Raman spectroscopy is still dominated by a resonance process which preferentially excites materials whose band gap matches excitation energy [25, 24]. Tuning excitation energies to higher values has been understood to resonate with σ bonds with a higher degree [25, 111], while lower excitation energies resonate better with the π bond [1, 80, 25]. If this holds true for the MWNT structure and other carbons, this offers an interesting approach to monitor modifications to π or σ bonds more closely by tuning excitation energy.

1.5 Overview of research

This study first establishes a new fitting procedure to reduce uncertainty in monitoring the G and D doublet characteristics in Chapter 2. A "standard" fit to the G and D doublet is re-assessed by using pseudo-Voigt functions and a variation of peak assignments. A new fitting procedure was found to lower uncertainty values for the most popular Raman

characteristics of the G and D doublet: the G band peak position and the D/G integrated intensity ratio.

To explore the enhancement of CNT composites through Raman spectroscopy, Chapter 3 contains a study that monitors the evolution of a MWNTs microstructure throughout an entire manufacturing process with the G and D doublet. Starting with purification, functionalization, and assembly into a final nano-composite, the Raman spectrum was recorded in an ex-situ fashion in between every processing step. Optimizing techniques are suggested using the G and D doublet characteristics. Finally, optimization of processing parameters was conducted using Raman spectroscopy for a laser sintering process. Raman spectroscopy revealed the most optimal operating parameters for the laser sintering process.

In Chapter 4, an experiment using multiple wavelength spectroscopy was conducted to investigate how this relatively new and advanced experimental technique can be used to assess microstructure strain and disorder. A pressurized filtration process, which induces a hydrostatic stress on the MWNTs changed the DRR properties significantly. A competition between C-C force constants and the DRR process was observed, where for higher excitation energies, the C-C force constants overcame the DRR effects. Results indicate that using higher excitation energies can avoid the DRR effects, by probing deeper into σ bonds, representing a more accurate measurement for microstructural strain.

CHAPTER 2
INVESTIGATION OF IMPROVED FITTING TECHNIQUES USING THE *PSEUDO*-VOIGT FUNCTION

2.1 Objective

Throughout literature, current Raman analysis methods have used different line-shape functions to interpret the G and D doublet. The combination of varying the number of peaks fitted and line shape functions used will be referred henceforth as "peak assignments". Various line-shape functions have been used in literature such as: pure Gaussian/Lorentzian (G/L) [67, 68, 2, 83], pure L [72, 48], pure G [98], Breit-Wigner-Fano/Lorentzian (BWF)/L [70, 38, 60], and *pseudo*-Voigt PV [30, 115, 123, 62, 18]. With multiple peak assignments referenced in literature, studies indicate that a more reliable curve-fitting technique is required [115] or that current methods are limited by the statistical uncertainty of parameters determined by curve fitting [83]. Here, the PV function [36] will be investigated as a fit for the Raman G and D doublet to develop an ideal curve fitting procedure based on the outcome and consistency of Raman characteristics. Raman characteristics are eventually quantified into stress, crystalline size, or effectiveness of functionalizations in the materials, and thus it is important to understand and minimize any uncertainties associated with the fitting process.

The Voigt profile [47], a convolution between G and L functions, is an important description of the symmetric features of spectral lines because of the practical goodness

of fit to experimental data [36]. This function takes into consideration the G and L characteristics contributed by a combination of broadening effects from thermal motion of atoms, particle size, and instrument factors [47, 100, 36, 106]. Pure G line-shapes are used for highly disordered carbons [98, 25], with extremely broad and rounded experimental profiles. Purely L line-shapes are commonly used for SWNT samples, because their experimental profiles involve sharp and narrow features [73, 79, 72]. G/L mixed shapes have been used more recently for hybrid carbons [30, 115, 123, 62, 18], such as MWNT nano-composites, that exhibit intermediate experimental profiles resembling both disordered carbons and SWNTs. Thus, a fit using a combination of G/L functions seems most appropriate for investigating the spectra of these novel carbon materials which contain a variety of carbon species.

The BWF function has been used to represent the G band for SWNTs [45, 11, 38, 104, 70, 65]. The presence of this asymmetric lineshape has been attributed to a resonance with metallic CNTs [45] as the product of an interaction of a phonon with a continuum of states [11] and also intrinsic with the formation of a band of plasmons within a bundle of SWNTs [38, 70]. The BWF function is normally not applied to CNTs with large diameters, such as the MWNTs studied here, but is a potential area of research for the future.

The G and D doublet was investigated in detail using a variety of peak assignments for the MWNT nano-composite studied here. In similar studies [83], optimum fits were selected based on minimum χ^2 values from a variety of carbonaceous materials. Here,

goodness of fit will be presented, however, optimum fits will be selected based on monitoring in-situ temperature relationships of Raman characteristics. Temperature relationships have been well documented for CNT structures and results from literature were compared to our results [55, 34, 102, 52, 81, 22, 104, 121, 33, 33, 59]. The purpose of this chapter is to provide and formulate alternative fitting procedures for the G and D doublet with a variety of peak assignments using the PV function.

2.2 Background

2.2.1 The pseudo-Voigt function

The pseudo-Voigt function, stemming from a Voigt profile [36, 106], was introduced by Wertheim et al. [112] and assumed equal linewidths of both G and L contributions. A parameter of this function, the Gauss ratio, determines the lineshape's G and L content [106]. Based on an assessment of several functions, Young et al. [116] determined the pseudo-Voigt to be a good approximation to the Voigt with the added benefit of improved computational time. This function was later developed for synchrotron X-ray spectra by Thompson [100], and it can be represented mathematically as follows:

$$\Phi(\nu) = 2A_l \left[\Phi_G(\nu) + \Phi_L(\nu)\right] \tag{2.1}$$

Where

$\Phi_G(\nu) = \frac{G}{W_l}\sqrt{\frac{\ln 2}{\pi}} \exp\left(-4\ln 2\left(\frac{\nu - C_l}{W_l}\right)^2\right)$

$\Phi_L(\nu) = \frac{L}{\pi W_l\left[1+4\left(\frac{\nu-C_l}{W_l}\right)^2\right]}$

ν is the emission wavenumber,

C_l is the peak position of the spectral line,

W_l is the FWHM of the spectral line,

A_l is the Area under the spectral line,

G and L are the Gaussian and Lorentzian shape factors respectively ($G = 1 - L$).

The above function is used to evaluate the intensity, $\Phi(\nu_i)$ at each of i spectral wavenumbers, ν_i and the sum of the intensities for all lines gives the convoluted spectrum with total intensity M_i at each spectral wavenumber as described in Eq. 2.2

$$M_i = \sum_{i=1}^{n} \Phi(\nu_i) \tag{2.2}$$

The goodness of fit (GOF) is quantified [90] by the merit function, $S = 1 - \omega$, where ω is described in Eq. 2.3. Hence, the merit function S approaches a perfect fit value of 1 with the minimization of the objective function ω. The deconvolution algorithm utilized in this study was performed with a Matlab-based genetic algorithm [77] for the optimization of fit using theoretical equations for the pseudo-voigt function described here.

$$\omega = \left\{ \frac{\sum_{i=1}^{n} \left(M_{i,\exp} - M_i\right)^2}{\sum_{i=1}^{n} \left(M_{i,\exp} - \overline{M}_i\right)^2} \right\} \tag{2.3}$$

The results of a benchmark experiment in Fig. 2.1 validate the superior fit, and also acted as a motivation for the rest of the experiment with multiple PV functions. The G and D doublet is of a unique and slightly asymmetric shape that could have several subbands hidden within. By carefully placing subbands within the G and D doublet to produce the best possible GOF, the GOF was investigated with an increasing number of subbands added. This process was done with PV, G, and L functions to emphasize the difference in GOF between the different functions. The fits settle down into a steady state after 7 peaks are assigned. This suggests that adding additional peaks past 7 would not benefit the fitting process. Later in the results section, a variable number of PV functions were fit to the G and D doublet and monitored during an *in situ* temperature experiment, and the benefits of the additional peaks are assessed.

2.3 Experiment

The sample used for this study was MWNT paper composed of tubes with 10-20 nm outer diameters, estimated using an SEM image (inset of Fig 2.2), and the sample was an intermediate phase of a nano-composite manufacturing process. The details behind the manufacturing of this sample are presented elsewhere [54]. Briefly, this thin, highly

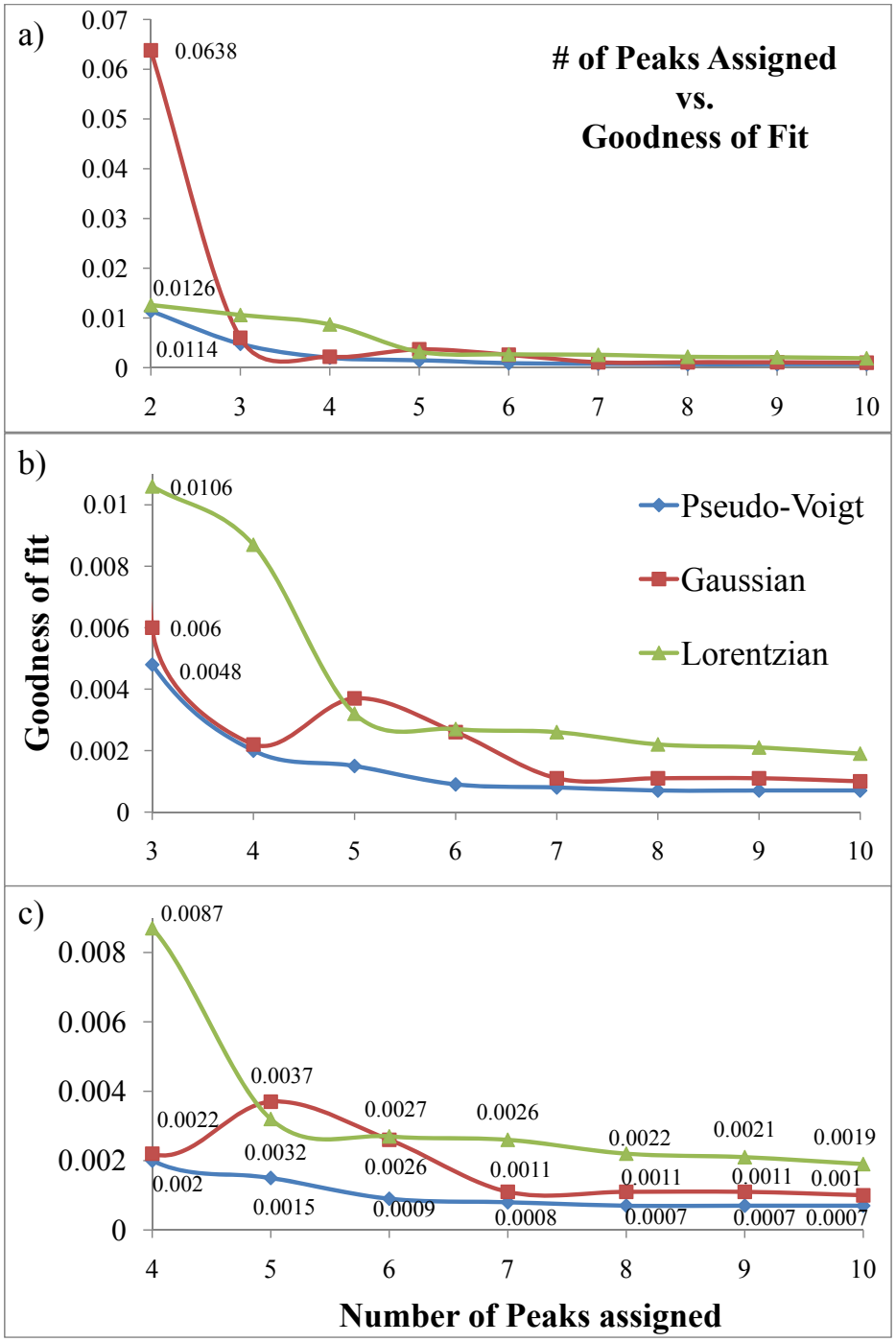

Figure 2.1: Benchmark experiment to prove the superior goodness of fit of the PV function compared to pure G and L functions. the three windows of a) b) and c) represent the same figrue, with different axis limits to enhance the clarity of steady state GOF.

condensed film of MWNTs was the product of a pressurized filtration process, with no host matrix present and with unfunctionalized, as-received MWNTs. Without a purification process prior to this filtration process, the presence of amorphous carbon and residual metal catalysts are likely. The manufacturing process of this MWNT thin film is discussed in detail in Section 3.2.

The Raman measurements were taken at the Center for Nanoscale Materials (CNM) at the Argonne National Laboratory (ANL). The Raman measurements were made using a 50X long working objective. A confocal Raman microscope (Renishaw inVia) was utilized with 514.5 nm excitation at a laser power of 9.5 mW, resulting in no laser-induced shifts in the Raman bands. The sample was mounted in a temperature-controlled stage (Linkam THMS600) held at 88K and increased to a temperature of 298K at a rate of 4 K/s, with data collected at every 10K. These temperatures were held for five minutes, which allowed the temperature to stabilize before each Raman measurement. In Fig. 2.2 a raw Raman spectrum of the G and D doublet frequency range was shown.

2.3.1 Parameters of the genetic algorithm

Controlling the GA's parameters were important to properly deconvolute the overlapping sub-bands and improve clarity of temperature relationships of the G , D, and D' peak positions. Constraints for all spectral parameters were left relatively open on the initial deconvolution with upper and lower bounds $\pm 30\%$, respectively, of initial guesses for area

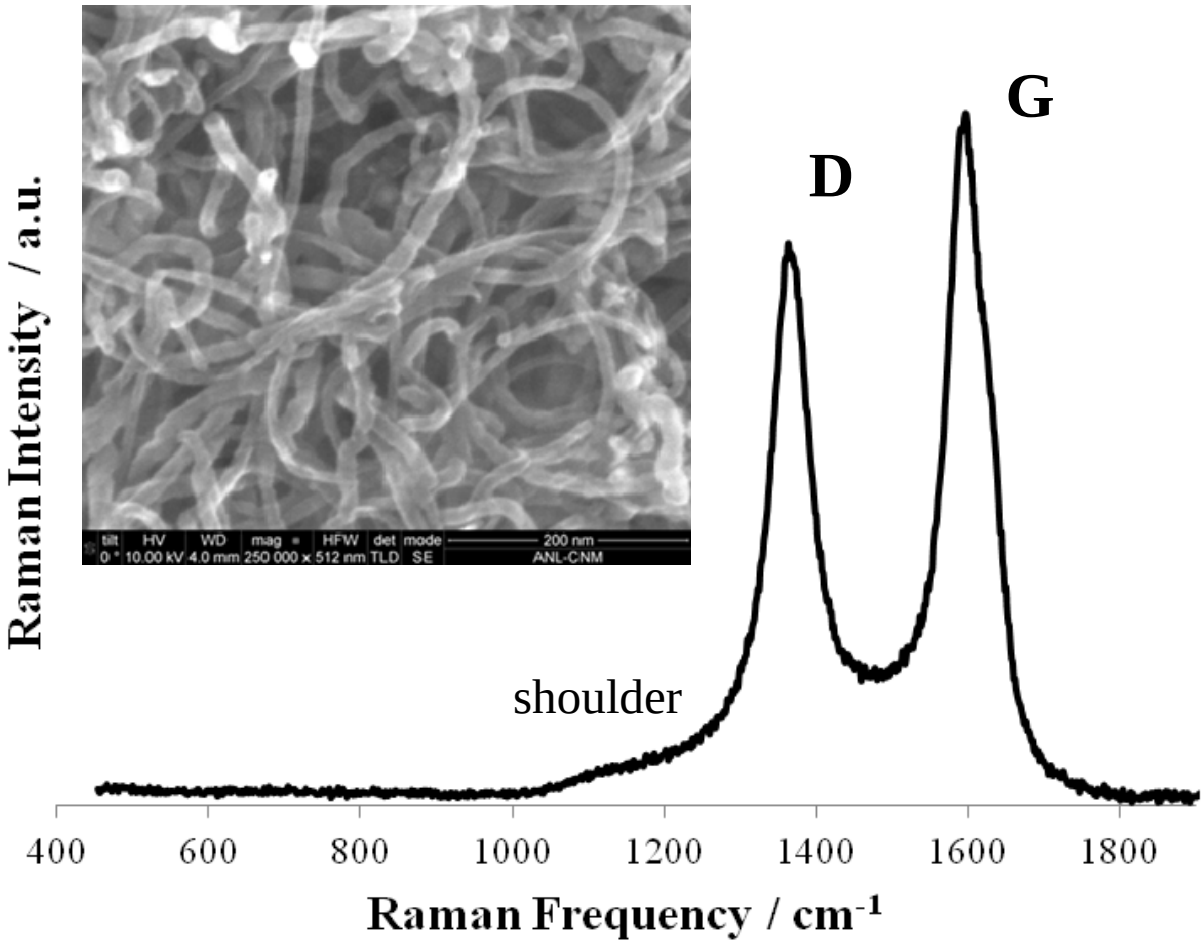

Figure 2.2: The raw experimental Raman spectrum of the G and D doublet for a MWNT thin film "Paper". The inset was an SEM image of the MWNT thin film.

Table 2.1: Average minimum fit and number of iterations to convergence due to BSA affinity for each peak assignment

Peaks	**Average gof**	**Average # of iterations**
7 PV	0.000756	2252
6 PV	0.000677	1341
5 PV	0.001042	795
3 PV	0.006492	443

and full width half max (FWHM). Peak positions were constrained much more due to the subtle 2-3 cm^{-1} Raman shift that was expected for the temperature regime studied. Thus, constraints for upper and lower bounds were $\pm 0.5\%$ respectively. After an initial deconvolution with these constraints, new constraints were assigned based on outputs for each variable across the temperature regime. Upper bounds increased and lower bounds deceased respectively by half with respect to the range of outputs for each variable in the first deconvolution. By tightening the constraints iteratively, the accuracy of the fitting increased, with a search of a much smaller design space for the global minimum in GOF.

The GA's bit string affinity (BSA) was held at 0.9 for this process, which was also set as the termination tolerance. To ensure that the convergence was solely due to BSA, the maximum number of iterations was set to a large value. For the additional PV functions assigned past three, it is believed that the complex overlapping of PVs made it difficult to converge, given the high number of average iterations in Table 2.1. Average fitness

values at convergence are also presented in Table 2.1. Surprisingly, 6 PV had a better GOF than 7 PV.

The results yield precise values for relatively distinct Raman features of G, D and D'. In addition, some of the sub-bands were found to have temperature dependencies. The results will focus on the peak position relationships of G, D, and D', and how they are affected by the presence of neighboring sub-bands based on the different fitting experiments.

2.3.2 PV peak assignments

Four different combinations of the pseudo-Voigt profile were adapted from literature and presented in Fig. 2.3 with linear baselines for all fits between 1000-1800cm^{-1}. The simplest 3 PV peak fit in Fig.2.3a was very similar to other deconvolutions done on MWNTs which used pure L functions for the G and D and a pure G function for D' [2, 93, 68]. This three-peak fit has been called standard [93] and includes the D' band that is normally present in MWNTs. A four-peak fit was initially attempted with an assignment of G, D, D', and a peak at $\approx$1400cm^{-1}, but the presence of this sub-band caused a convergence with an unconventional $I(D') > I(G)$ characteristic. This intensity ratio characteristic has only been reported for excitation wavelengths that are in the infrared region [2], and since visible excitation was used here; this four peak assignment was concluded to be unsuitable.

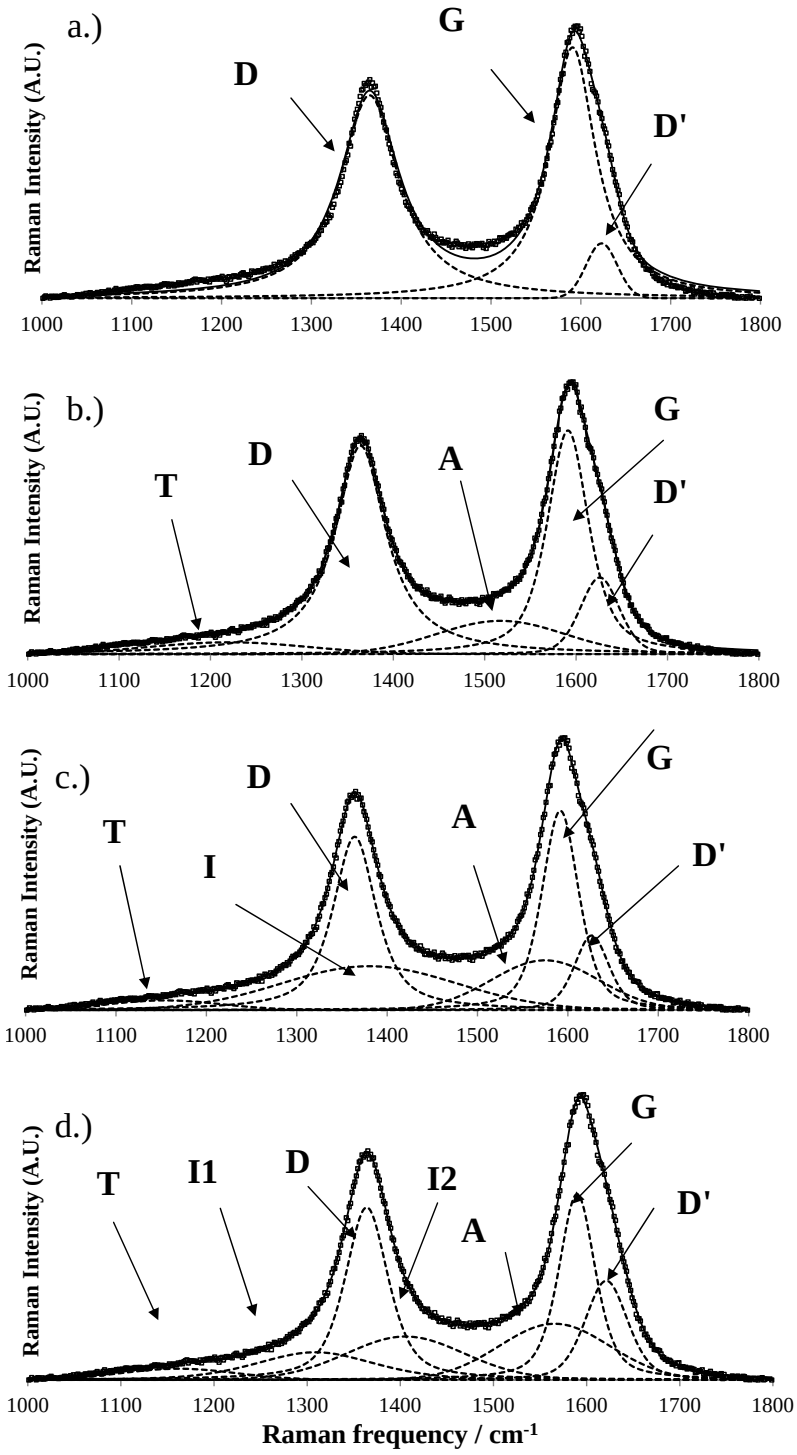

Figure 2.3: Deconvoluted Raman G and D doublet using the 3 PV (a.), 5 PV (b.), 6 PV (c.), and 7 PV (d.) peak assignments.

For the five, six and seven peak assignments, their adapted origins came mostly from literature of carbonaceous materials that had similar G and D doublet features [115, 123, 83]. These peak assignments all share two additional sub-bands with respect to the 3 PV. The addition of two peaks at ≈1150 and $1500cm^{-1}$ have been included in the deconvolution process for disordered and amorphous carbon [25] and for pyrolyzed wood [115, 123] as the T and A band, respectively. The T-band, at $\approx 1150cm^{-1}$, has been attributed to sp^3 bonding [115, 25] and is more distinct for ultraviolet (UV) excitation [25]. The A band at $\approx 1500cm^{-1}$, has been attributed to amorphous carbon for soot [83], but for densely packed double walled nanotubes (DWNT) samples, it was attributed to either metallic nanotubes or an overlapping of peaks from several different diameters [67].

The six and seven peak assignments contain an additional I band that has been used in a variety of carbons [83, 123]. For 6 PV, this peak was located at wavenumbers just higher than the D band. This I band has been deconvoluted in literature as a L function and has been attributed to a few different mechanisms including disorder, polyene chains, and ionic impurities [83]. For the 7 PV, the I band was broken into two peaks, I1 and I2, located at lower and higher wavenumbers with respect to the D band. With several origins of the I band possible [83], the I band was split into two components for 7 PV.

2.4 Results and Discussion

2.4.1 Gauss Ratios for various peak assignments

Each PV function assigned provided an output of 5 Raman characteristics: Intensity, Integrated Intensity, full width half max (FWHM), peak position, and Gauss Ratio (GR). The GR for every peak in each peak assignment was plotted vs. temperature in Fig. 2.4 except for the 3 PV fit. The 3 PV fit converged to 2 pure L (G and D bands) and a pure G (D' band), which matches up with literature where the same "standard" fit [93, 1] was used. A few studies utilized the PV function [4, 123], however this is the first known report of the GR.

The rest of the peak assignments (5, 6 and 7 PV) provided an output of different GRs with different degrees of uncertainty. The 7 PV had the most uncertain GR values, due to the high number of peaks assigned. On average, the PV functions in the 7 PV fit had slightly higher GRs compared to the 5 and 6 PV fits. The 5 and 6 PV peak assignments had GRs that were decreasing as the number of PV functions decreased. The need to account for the absence of PV functions was provided by the "tails" of the L functions. It is also noted that the 5 PV peak assignment's D band converged to a L function, similar to that of the so called "standard" 3 peak fit in literature [93, 1].

The 6 PV fit provided the most consistent GR values with the lowest uncertainty for the Raman bands of interest in MWNT nano-composite studies (G, D and D'). The rest

of the peaks assigned in the 6 PV fit converged to G functions. The average G band GR was 0.44±0.021, 0.45±0.010, and 0.24±0.014 for 7, 6, and 5 PV fits respectively.

2.4.2 Varying D/G ratios with peak assignment

Crystallite size for the basal plane, L_a, has been estimated using intensity [123] and integrated intensity [25] ratios of the G and D bands. However, errors have been reported to be as large as 100% when compared with X-ray diffraction [17]. Here, we cannot verify what peak assignment yielded the most accurate L_a because complementary X-ray measurements were not taken, but qualitative comparisons to literature can be made. Even without obtaining values, the D/G value can still be used to determine qualitative increases in the crystallite size, L_a. The addition of sub-bands within the G and D doublet or discrepancies in line-shape function could greatly affect the outcome of any D/G ratio [123]. Using Eq. 2.4, a rough estimate of L_a was calculated, primarily to observe any discrepancies that resulted from various peak assignments. E_l represents the laser excitation energy and $\frac{I'_D}{I'_G}$ represents the ratio of integrated intensities of G and D.

$$L_a(nm) = 560/{E_l}^4(\frac{I'_D}{I'_G})^{-1} \tag{2.4}$$

All PV fits had varying L_a values depending on the peak assignment. This emphasizes the importance of peak assignments in Table 2.2. The D/G integrated intensity ratios were averaged over the temperature data as no clear relationship was found for this

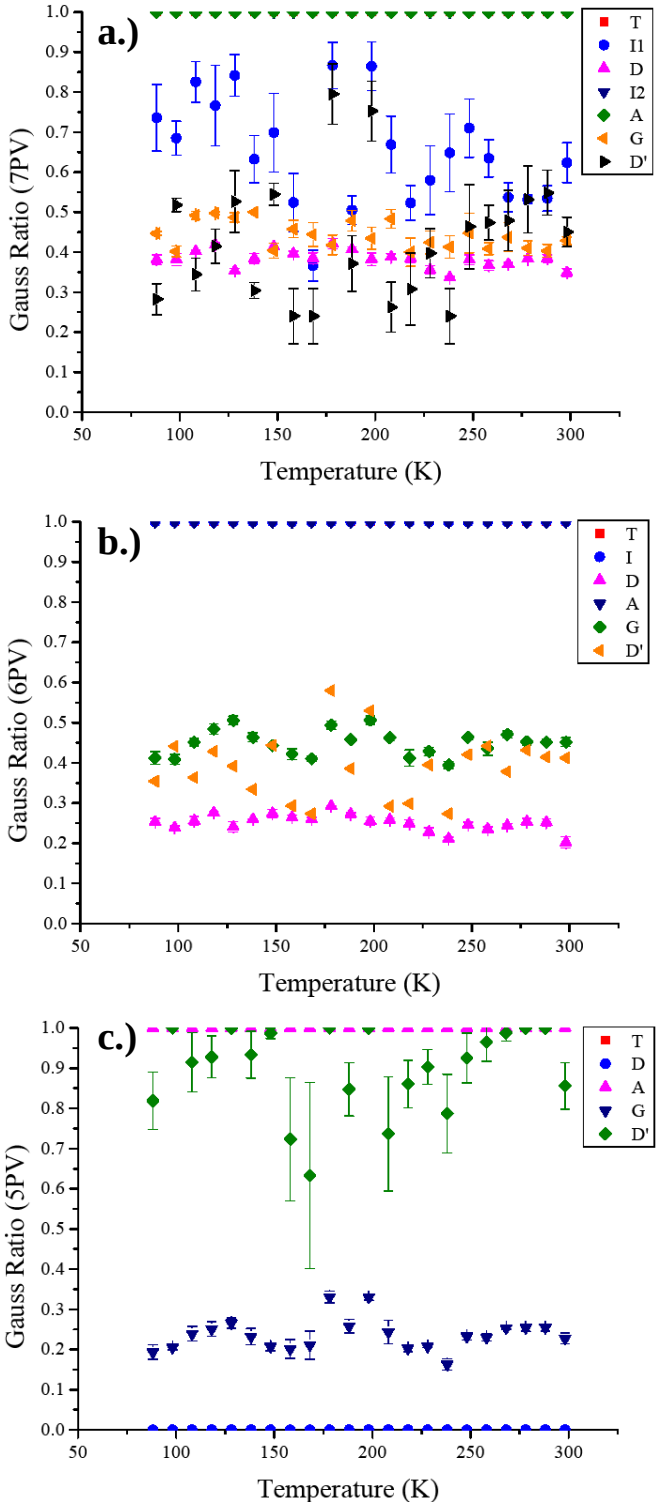

Figure 2.4: The temperature dependencies of 7 PV (a.) 6 PV (b.) and 5 PV (c.) Gauss Ratios (GRs). Error bars represent standard deviation for 3 deconvolutions.

Table 2.2: Calculating L_a values based on D/G integrated intensity ratio

	Equation 4	
Peaks	L_a**(nm)**	U_{L_a}**(nm)**
7 PV	15.390	+/- 0.460
6 PV	15.116	+/- 0.299
5 PV	12.945	+/- 0.280
3 PV	17.354	+/- 0.515

temperature regime (88-298K). Table 2.2 displays the results of crystallite size, L_a, as well as the systematic uncertainty, U_{L_a}. Crystallite sizes are of the same order, but considerably smaller than those reported by Soin *et al.* [93], who applied Eq. 2.4 to vertically grown MWNTs using the three peak fit. Soin *et al.* calculated $L_a \approx$30-60nm depending on growth parameters [93]. The smaller size reported here, where $L_a \approx$12-17nm could be attributed to the high density of the MWNTs, which could create tube-tube defects and presence of amorphous carbon.

The 5 PV peak assignment had the lowest systematic uncertainty, closely followed by 6 PV. Therefore, the 5 or 6 PV fit would be most desirable if one was attempting to compare L_a qualitatively. Despite their low uncertainties, there was a difference between the two L_a values for 5 and 6 PV, yielding 12.945 and 15.116 nm respectively; limiting their use to only be qualitative. Eq. 2.4 was applied to CNTs using a 3 peak assignment that was similar to the 3 PV studied here by Soin *et al.* [93]. This yielded the highest

value of uncertainty for L_a in Table 2.2. Future work should involve the formulation of an empirical relationship to quantitatively relate parameters of the G and D doublet to L_a using the 5 PV peak assignment.

2.4.3 Temperature dependent peak positions of D, G and D' bands

The G and D doublet was studied here for the temperature range (88K-298K), with an emphasis on the transition between the two temperature regimes of T_c and T_h. The transition was relatively higher for the MWNT thin film (238K) compared to the transitions of other studies (150K) [33]. The relatively high transition temperature could be indicative of an environment with a high density of MWNTs, with the absence of a host matrix, and where only a small fraction residual particles and amorphous carbons transfer strain between the MWNTs.

In order to determine the most appropriate peak assignment for accurately determining these shifts in peak positions, a linear function was fit to each temperature regime of T_h and T_c. This technique is similar to work from Vega *et al.*, who fit a linear function above and below the glass transition temperature (T_g) [105]. The relationships for the T_c regime were not available for comparison from literature for any of the peaks studied, however $\frac{\Delta\omega}{\Delta T_c}$ values are presented for this study in Table 2.3.

The proximity of the experimental $\frac{\Delta\omega}{\Delta T}$ values recorded here and literature was used to help determine the most suitable peak assignment. However, CNT materials' $\frac{\Delta\omega}{\Delta T}$ have

been known to fluctuate with different tube types [34]. Thus, two additional parameters were used for each peak assignment: the linear correlations to experimental data for each linear fit (R^2), and the average standard deviation of peak position ($\overline{\sigma}_\omega$). $\frac{\Delta\omega}{\Delta T}$ values and R^2 values are given in Table 2.3 for each temperature regime. Table 2.4 includes $\overline{\sigma}_\omega$ values for G, D, and D'.

The experimental $\frac{\Delta\omega_G}{\Delta T_h}$ values were lower for all peak assignments with respect to literature, which used pure L functions, and obtained $\frac{\Delta\omega_G}{\Delta T_h}$ ranging from -0.026 to $-0.023\ cm^{-1}/K$ [22, 34]. 3 and 7 PV were closest to literature, both with values $-0.019\ cm^{-1}/K$, while 5 and 6 PV both had a lower value of $-0.014\ cm^{-1}/K$. All peak assignments had linear correlations of the same order; with 3 PV being the best, followed by 6 PV.

The $\frac{\Delta\omega_D}{\Delta T_h}$ and $\frac{\Delta\omega_{D'}}{\Delta T_h}$ experimental values were larger for all peak assignments with respect to literature, opposite from the decrease observed for $\frac{\Delta\omega_G}{\Delta T_h}$. $\frac{\Delta\omega_D}{\Delta T_h}$ values were all of the same order, with 3 and 6 PV having the closest values resembling those reported in literature of $-0.019\ cm^{-1}/K$ [22]. The best linear correlations belonged to 7 and 5 PV. As for $\frac{\Delta\omega_{D'}}{\Delta T_h}$ values, 5 and 6 PV had the closest temperature relationships with respect to literature of $-0.029\ cm^{-1}/K$ [22], while 3 and 7 PV were much larger. Most accurate R^2 values for $\frac{\Delta\omega_{D'}}{\Delta T_h}$ belonged to 3 and 5 PV.

Values concerning $\frac{\Delta\omega}{\Delta T_h}$ and their respective R^2 favored various peak assignment for G, D and D' peak positions. Therefore, it is not possible to make distinct conclusions about the most appropriate peak assignment based on comparing our experimental values to

Table 2.3: Peak position temperature relationships for G, D and D' for both the T_c and T_h temperature regimes.

	88-238K		**248-298K**	
	$\frac{\Delta\omega}{\Delta T_c}$, $(\frac{cm^{-1}}{K})$	R^2	$\frac{\Delta\omega}{\Delta T_h}$, $(\frac{cm^{-1}}{K})$	R^2
	G band position			
7 PV	-0.002	0.045	-0.019	0.682
6 PV	-0.003	0.077	-0.014	0.704
5 PV	-0.002	0.078	-0.014	0.632
3 PV	-0.007	0.294	-0.019	0.750
	D band position			
7 PV	-0.004	0.349	-0.022	0.574
6 PV	-0.005	0.393	-0.020	0.474
5 PV	-0.005	0.404	-0.021	0.592
3 PV	-0.005	0.359	-0.020	0.498
	D' band position			
7 PV	-0.005	0.037	-0.038	0.738
6 PV	-0.002	0.046	-0.029	0.655
5 PV	-0.001	0.006	-0.030	0.804
3 PV	-0.010	0.442	-0.038	0.940

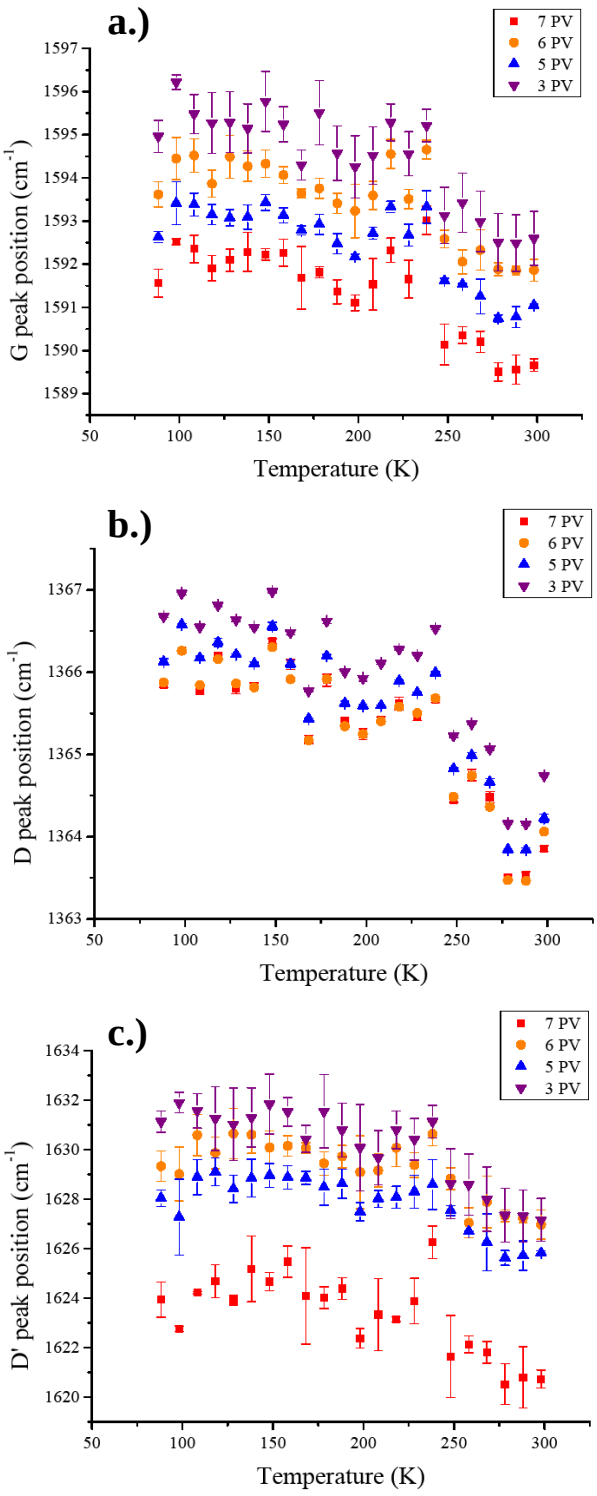

Figure 2.5: The temperature dependencies of G (a.) D (b.) and D' (c.) peak positions. Error bars represent standard deviation for 3 deconvolutions.

Table 2.4: Average uncertainties for G, D, and D' peak positions for three repeated deconvolutions

Peaks	$\overline{\sigma}_{\omega_G}$	$\overline{\sigma}_{\omega_D}$	$\overline{\sigma}_{\omega_{D'}}$
7 PV	0.306	0.046	0.694
6 PV	0.300	0.017	0.643
5 PV	0.197	0.024	0.554
3 PV	0.567	0.014	1.020

literature. Additional evidence for developing the most appropriate peak assignment were found with uncertainty values, $\overline{\sigma}_{\omega}$, in Table 2.4. These uncertainty values were calculated as the average size of the error bars in Fig. 2.5 for the entire temperature regime, for 3 repeated deconvolutions. The $\overline{\sigma}_{\omega}$ values provide consistent evidence for supporting 5 PV as the most appropriate peak assignment for ω_G and $\omega_{D'}$, while 3 and 6 PV were very close for the most consistent peak assignment with respect to the ω_D value. By inspection of Table 2.4, $\overline{\sigma}_{\omega_D}$ was of almost an order of magnitude smaller than $\overline{\sigma}_{\omega_G}$ and $\overline{\sigma}_{\omega_{D'}}$, and thus minimizing the uncertainty for ω_G and $\omega_{D'}$ with the 5 PV assignment was of greater significance.

2.4.4 Temperature dependent FWHM of D, G and D' bands

The D-band width was a Raman characteristic that is very sensitive to peak assignment. A previous study by Zickler *et al.* [123] compared the D band width, γ_D, against heat treatment times in pyrolyzed spruce wood using a 5 PV and a 2 PV fit. A large enhancement of γ_D by about 400% from the 2 PV to the 5 PV fit [123] was observed. Here, the enhancement was about 30% between the 5 PV and 3 PV fit because our D-band is much sharper and distinct than for the spruce wood. Significant differences still remained in the various peak assignments presented in Fig. 2.6 for γ_D. The D band appears to be linear with temperature for the 3 PV fit in Fig 2.6b, however with the addition of more PV functions the relationship appears contain two different regimes T_c and T_h before and after the transition ≈228 K. Past this transition temperature, the D band width seems to have a linear relationship with temperature, with the slope values presented in Table 2.4 for each peak assignment.

In situ temperature data for γ_D has not been studied in literature as much as ω_G because it is not related to the C-C stretching modes, but instead related to various defective sites on the surface of the CNT. Here its values were reported because distinct differences were observed for $\frac{\Delta\gamma_D}{\Delta T}$ between the two temperature regimes. Unfortunately no values for $\frac{\Delta\gamma_D}{\Delta T}$ for either temperature regime are known to compare with, so linear correlation for the two regimes were used to measure the consistency of the peak as-

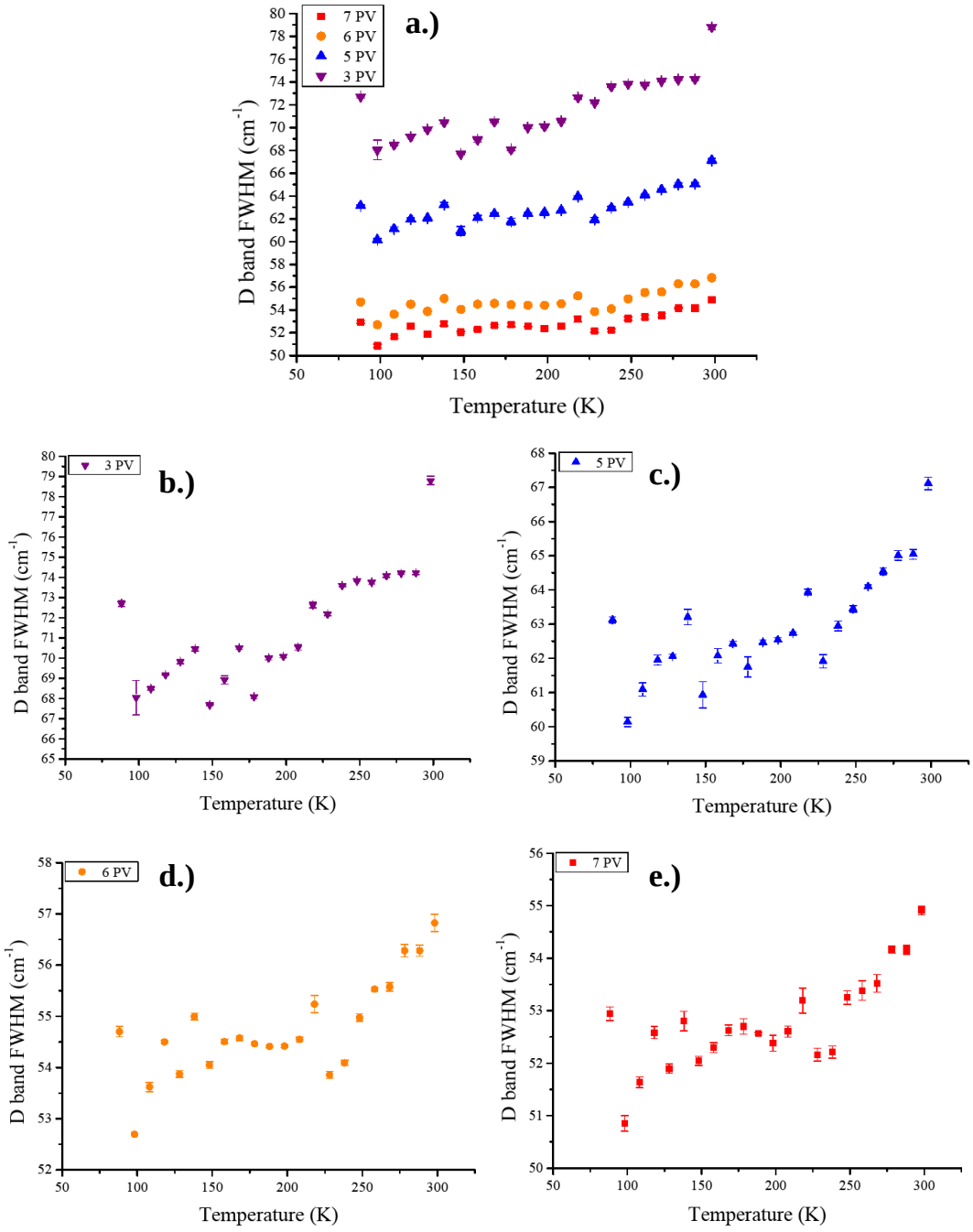

Figure 2.6: The temperature dependencies for the D band width for all peak assignments (a). Enhanced views for the 3 PV (b), 5 PV (c), 6 PV (d), and 7 PV (e) peak assignments. The error bars represent the standard deviation for 3 repeated deconvolutions.

signments in Table 2.4. Uncertainty for γ_D averaged out over both temperature regimes ($\overline{\sigma}_{\gamma_D}$) in Table 2.5 to compare as well.

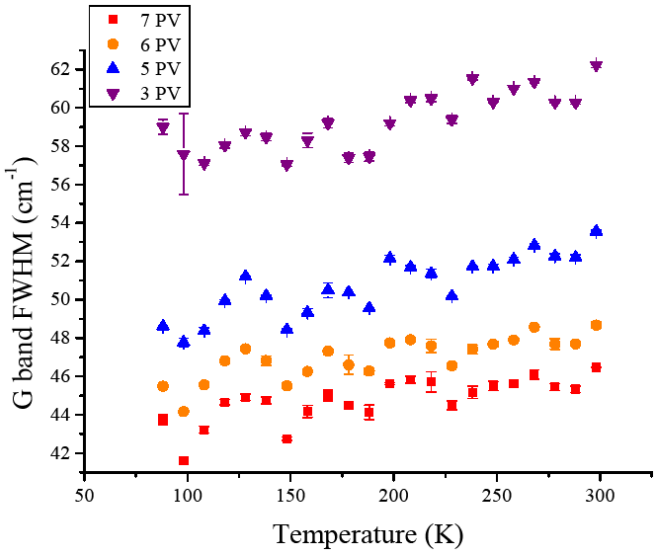

Figure 2.7: The temperature dependencies for the G band width for all peak assignments. The error bars represent the standard deviation for 3 repeated deconvolutions.

The G band width temperature relationship $\frac{\Delta\gamma_G}{\Delta T}$ was observed to have a linear trend for the entire temperature regime. No transition was observed for the temperature range observed here. $\frac{\Delta\gamma_G}{\Delta T}$ values were available for comparison on studies with SWNTs and DWNTs which had values to be 0.012 and 0.020 extrapolated from references [121, 104]. The DWNT $\frac{\Delta\gamma_G}{\Delta T}$ value was substantially higher than for SWNTs in Ref [121, 104]. MWNTs were recorded here, and it should be expected that the $\frac{\Delta\gamma_G}{\Delta T}$ values reported should resemble the DWNTs more than the SWNTs.

Table 2.5: D and G band FWHM temperature data

	88-218K		**88-298K**		**228-298K**	
	$\frac{\Delta\gamma_D}{\Delta T_c}$ $(\frac{cm^{-1}}{K})$	R^2	$\frac{\Delta\gamma_D}{\Delta T_h}$ $(\frac{cm^{-1}}{K})$	R^2	$\frac{\Delta\gamma_G}{\Delta T}$ $(\frac{cm^{-1}}{K})$	R^2
7 PV	0.005	0.160	0.039	0.955	0.013	0.547
6 PV	0.005	0.144	0.044	0.961	0.013	0.600
5 PV	0.010	0.207	0.061	0.922	0.021	0.724
3 PV	0.012	0.106	0.063	0.588	0.019	0.628

From inspection of Table 2.4, Table 2.5 and Fig. 2.6, the most accurate peak assignments for $\frac{\Delta\gamma}{\Delta T}$ values was between 5 and 6 PV because they produced the lowest $(\overline{\sigma}_\gamma)$ values for G and D band respectively. From Fig. 2.6, a dynamic relationship for $\frac{\Delta\gamma_D}{\Delta T}$ was produced for all fits other the the "standard" fit of 3 PV. The 5 PV fit produced $\frac{\Delta\gamma_G}{\Delta T}$ values which match better with references that suggest values for the MWNT sample should be more similar to DWNTs rather than SWNTs [121, 104]. With the other fits failing to achieve $\frac{\Delta\gamma_G}{\Delta T}$ values larger than for DWNTs, here we conclude the 5 PV peak assignment was most accurate for monitoring γ values.

2.4.5 Temperature dependent subbands of G and D doublet for MWNTs

Subbands have not yet been known to be within the MWNT G and D doublet, but they offer opportunity to extract additional information about the MWNT microstrucutre.

Table 2.6: Average uncertainties for G, D, and D' FWHM for 3 repeated deconvolutions

Peaks	$\overline{\sigma}_{\gamma_G}$	$\overline{\sigma}_{\gamma_D}$	$\overline{\sigma}_{\gamma_{D'}}$
7 PV	0.206	0.122	1.567
6 PV	0.150	0.070	0.357
5 PV	0.110	0.142	0.663
3 PV	0.247	0.128	2.213

The subbands reported here, were deconvoluted in the 6 PV fit in Fig. 2.8. The 5 and 7 PV fits' subbands did have some noticable temperature dependencies, however the 6 PV emphasized their temperature relationships better. The T band, related to sp^3 vibrations [115, 83] and more noticeable for UV excitations [111], did not have any noticeable temperature dependencies. The A band has been related to a vibrational mode of amorphous carbon [83], and the I band has been related to the intercalation of ions in the graphitic walls [115, 83], and both had pronounced temperature relationships in Figure 2.8. The 6 PV fit had the most promising subband relationships with temperature. Debatable temperature dependencies will not be discussed here, however the selected characteristics of the 6 PV's I and A bands will be discussed.

The A band's peak position temperature relationship was observed in Fig. 2.8b. The A band's temperature relationship was very similar to that of the G, D, and D' bands observed in Section 2.4.5, where little to no change occurs in the cold temperature regime (T_c), and after the transition temperature at ≈238K, the peak position begins to decrease

with a slope of ≈-0.036 cm^{-1}/K. This value is larger than the temperature relationship reported for the G band in section 2.4.3. It is normal to see disorder and amorphous carbon having larger $\frac{\Delta\omega_G}{\Delta T}$ values than for MWNTs [22]. This temperature relationships confirms the identity of this subband and could potentially allow for a quantification of amorphous carbon with respect to intrinsic MWNT vibrations using an integrated intensity ratio $\frac{I'_A}{I'_G}$.

Resolving the I band with temperature could lead to possible applications to monitoring the functonalization of the MWNTs because of its association with particles and ions within the graphitic walls of CNTs [115, 83]. By inspection of the FWHM temperature relationship in Fig. 2.8c, there appears to be a minimum in FWHM at ≈150K. This may be a indicator of the penetration of N_2 molecules that were used to cool the MWNT thin film to extremely low temperatures. Another property of the I band, was the I-1 band's peak position relationship for the 7 PV fit. A global critical point was observed for peak position, just as the I band's FWHM for the 6 PV fit. This band shows promise for future applications of *in-situ* functionalization studies.

2.5 Conclusion

The pseudo-Voigt function, in combination with new sub-bands to the MWNT analysis, provided resolvable Raman-temperature relationships for ω_G and D/G integrated intensity ratios with good fits. Calculating residual stress and identifying the transition

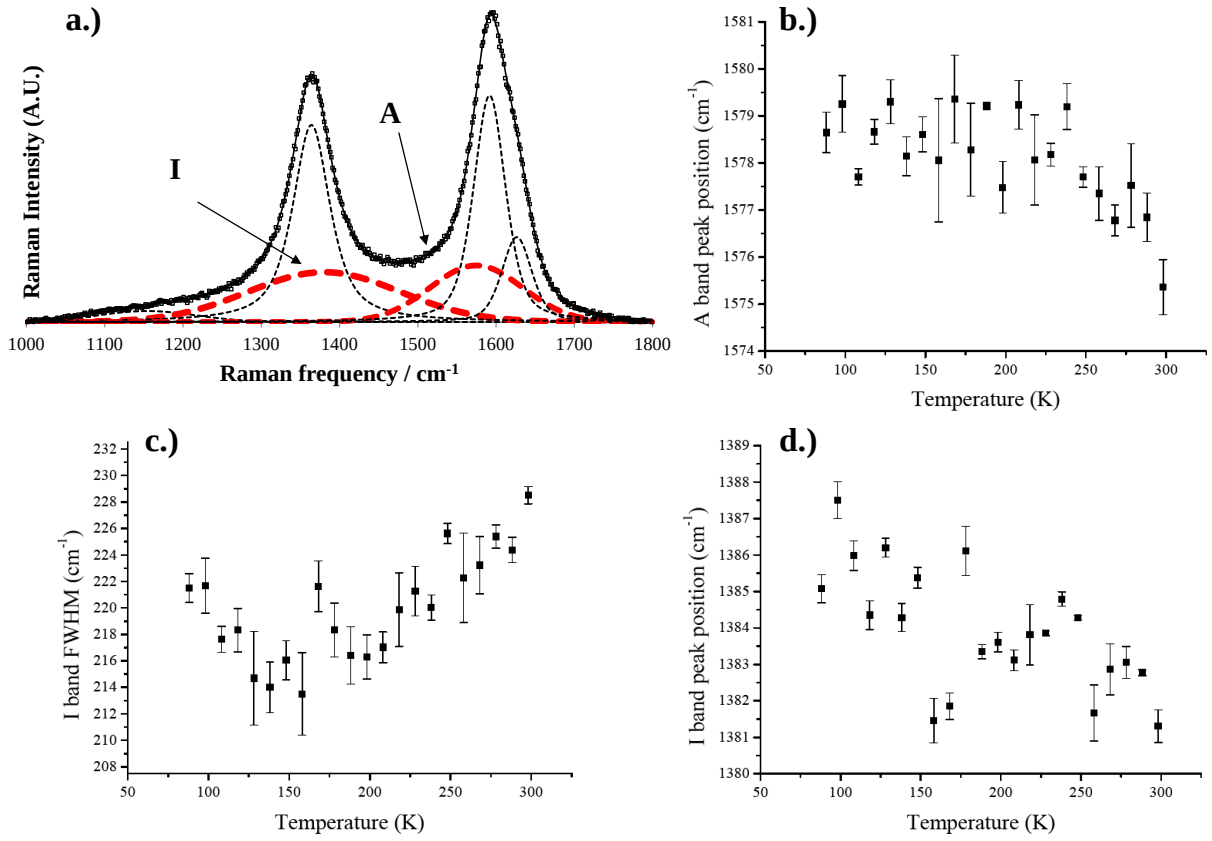

Figure 2.8: The deconvoluted G and D doublet for (a) the 6 PV peak assignment. (b) The A band peak position, (c) the I band FWHM, and (d) peak position all from the 6 PV peak assignment.

temperature where $\frac{\Delta\omega_G}{\Delta T}$ changes are important because these can define the strength of a CNT composite [55, 33]. Despite various evidence supporting each peak assignment, the most desirable consistencies for Raman analysis for CNTs are with ω_G and D/G since they are used extensively to assess CNT composite properties. With this in mind, the 5 PV provided the most reliable fit for the G and D doublet for both of these Raman characteristics.

The $\frac{\Delta\gamma}{\Delta T}$ values are not as established in literature, with comparisons only available for SWNTs [104] and DWNTs [121]. However, results indicate that γ_D had a dynamic temperature relationship that was revealed with the consideration of additional PV functions into the G and D doublet, while this relationship was masked for the "standard" fit. These new peak assignments open the door for additional studies of the relationship of γ_D with respect to physical properties such as MWNT diameter distribution [2].

However, monitoring the GA parameters in Table 1, the 6 PV fit was interesting in regards to the low gof it produced compared to all other peak assignments. The 6 PV fit consistently performed second best for L_a and all $\overline{\sigma}_\omega$ values, while performing best for $\overline{\sigma}_{\gamma_D}$ and $\overline{\sigma}_{\gamma_{D'}}$ values. The 6 PV was also the showcased fit for Section 2.4.5, which investigated the temperature relationships for the subbands. For future work, the 6 PV may be a candidate for further investigation.

Determining the merit for each peak assignment may also require consideration of the consistences within the sub-bands' characteristics, such as the T, I, or A bands. The sub-bands could yield valuable information about the variously hybridized microstructure of

a CNT sample. However, sometimes a simple 3 PV deconovlution could be more practical if such detailed information is not desired. This "standard" 3 PV deconvolution would take less computing power and time, but the increased uncertainty of peak positions would also be adopted. Future work is required on relating physical properties for CNT structures to the G and D doublet. This study suggests the 5 PV peak assignment is the most promising for future studies, yielding the most consistent ω_G, γ_G, and D/G characteristics.

CHAPTER 3
OPTIMIZING THE MANUFACTURING PROCESSES OF CNT-COMPOSITES WITH RAMAN SPECTROSCOPY

3.1 Objective

This chapter will investigate the manufacturing process for selected CNT composites through systematic characterization. The goal is to investigate and propose optimization techniques by monitoring trends in Raman characteristics for various manufacturing parameters. Carbon nanotubes (CNTs) have been added as reinforcing fibers to nanocomposites ever since they were investigated by Ijima et al [37]. These super strong CNTs are promising reinforcements, with a Young's modulus theoretically [82] and experimentally [117] calculated at the nano-scale to be approximately 1 TPa. However, they have yet to reach their full potential for mechanical strength when manufactured as nano-composites.

Challenges in developing CNT composites arise from inefficient load transfer to the nanotubes caused by slippage between the fiber-matrix interface [57]. CNTs also tend to agglomerate, and agglomerates of CNTs can act as stress concentration points reducing the mechanical properties of the nano-composites [61]. The concept of functionalizing the CNTs by grafting chemical groups on its surface which act as anchors between the fiber-matrix interface, and using dispersion agents, have helped the progress of improving mechanical properties of CNT-composite [107, 122]. Proper functionalization and

assembly of CNTs need to be investigated in detail to discover optimal conditions for manufacturing of nanocomposites. The ability to use a consistent method to monitor the microstructure changes of CNTs over an entire manufacturing process, such as Raman spectroscopy, can potentially allow for the tailoring of these nanocomposites to optimize specific properties.

In this chapter, emphasis will be given to the G and D bands. The G and D doublet feature has been used to quantify defect density on the CNT's surface using the D/G ratio of integrated intensities [4]. This ratio will be used to qualitatively relate defect concentrations on the MWNT surface across the different stages of the manufacturing processes. The G band position can also quantify stress of both hydrostatic [108, 60] and uni-axial [51, 28] types, with up-shifts or down-shifts in peak position of the G band respectively. These above properties can be extracted from a relatively narrow frequency range on the Raman spectra that encompasses the G and D doublet (1200-1700cm^{-1}). Other bands in the Raman spectra exist that could potentially yield additional information, such as a second order defect induced band, D'(1610cm^{-1}). This has been used as an indicator of covalently attached particles to the MWNT side walls [15]. However, this study will focus on the more commonly known G and D band characteristics in detail.

3.2 Background for processes studied

Since the application of this Raman optimization technique depends highly on the material manufacturing processes. The results must be given context by first introducing the separate manufacturing processes studied, and giving definition to all of the samples studied. Two different application of this technique were investigated, the first being an examination of the microstructure evolution throughout a polymer based MWNT composite manufacturing process, and the second being a study on specific processing parameters for laser sintering on a ceramic based MWNT composite. The starting constituents for all materials in this section were multi-walled carbon nanotubes (MWNTs), which were received from Nanolab, Inc. (length: 5-20 $/mu$m).

The manufacturing process was studied in an ex-situ fashion starting with as-received MWNT constituents (CNT-P) up to the final product that was a multi-functional polymer nanocomposite (NC-F) [54]. This process includes the functionalization of the MWNTs using polyhedral oligomeric silsequioxane (POSS). Then the rest of the manufacturing processes included the functionalized MWNTs, in addition to a control variable of pristine MWNTs.

The second process studied, was a detailed examination of a single phase of a different manufacturing process for a ceramic based MWNT composite. This material would be eventually applied to a rocket combustion coatings, allowing for the combustion of

propellants at higher temperatures [29]. Specific manufacturing parameters for laser sintering of a MWNT-TiO_2 mixed paper were optimized with Raman spectroscopy.

3.2.1 MWNT-compsite: Oxidation and functionalization

The as-received CNTs (CNT-P) were oxidized with a mixture of nitric acid (HNO_3) and sulfuric acid (H_2SO_4) in an ultrasonic bath. The oxidized CNTs (CNT-O) were dried and then grinded into powder with a mortar. A mixture of acid-modified CNTs, thionyl chloride ($SOCl_2$ with large amount) and N, N-$dimethylformamide$ was dispersed in an ultrasonic bath. The residual $SOCl_2$ was removed by the reduced pressure distillation method to yield acyl chloride functionalized CNTs (CNTs-$COCl$). The CNTs-$COCl$, POSS-NH_2 and Et_3N as catalyst were added in a glass flask and dispersed by $CHCl_3$. The mixture was suspended in an ultrasonic bath, and stirred by magnetic stirrer in an oil bath under high purified N_2 atmosphere. The product obtained was vacuum-filtered and washed five times with excess $CHCl_3$ to remove the residual of POSS molecules then dried to yield neat POSS-g-CNT (CNT-F).

3.2.2 MWNT-compsite: Pressurized filtration

The functionalized CNTs(CNT-F) were transferred into a 1000mL beaker and 400 mL of deionized water was added. The solution was sonicated, then cooled down to room

temperature and a surfactant was added into the solution. The solution was sonicated again and then cooled down to room temperature. Finally, the as-prepared suspensions were sonicated briefly and immediately transferred into a filtration system.

The CNT paper was made by filtering the suspension through 0.4μm hydrophilic polycarbonate membrane under a high-pressure filtration system. Once the paper was made, the filter with the CNT paper was carefully removed and placed onto another piece of paper where the filter was detached. The remaining CNT paper was dried in an oven. This process was done separately for two different CNT powder constituents, CNT-P and CNT-F. The products of this pressurized filtration was Paper-F and the control sample, Paper-P as seen in Fig. 3.1.

3.2.3 MWNT-compsite: Resin infusion

Vacuum-assisted resin transfer molding (VARTM) process has been widely used to produce low-cost, high quality, and geometrically complicated composite parts. In this study, the VARTM process was used to fabricate the CNT paper based nanocomposites, which were carried out in three steps. In the first step, CNT papers, (Paper-P and Paper-F) were placed on the bottom half of a mold. After that, a peel ply, resin distribution media, and vacuum bag film were placed on the top of fiber mats. The vacuum film bag was then sealed around the perimeter of the mold and a vacuum pump was used to draw a vacuum within the mold cavity. The next step was the mold filling during which

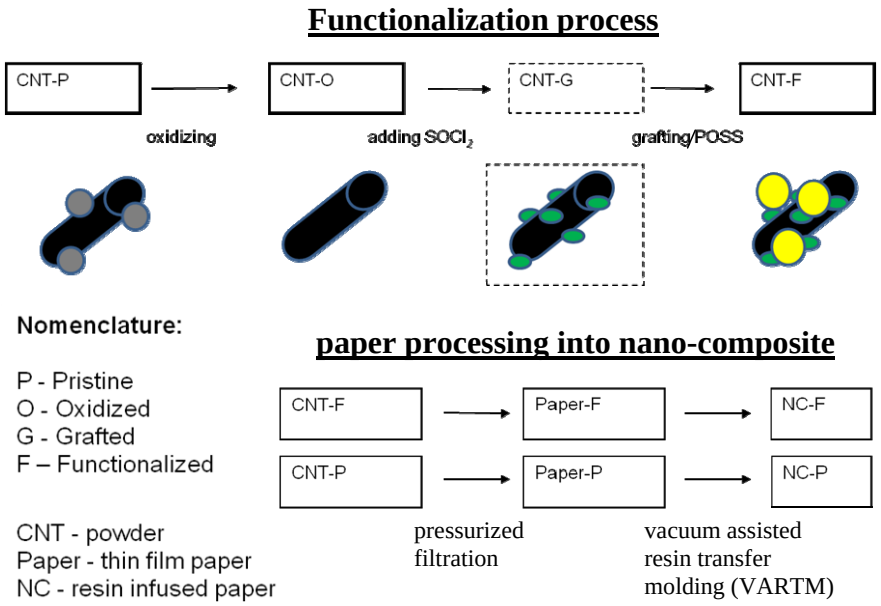

Figure 3.1: Summary of all intermediate samples of the manufacturing process, split into two main processes: functionalization and paper processing. The dotted lines around CNT-G indicates an intermediate stage that was not studied here.

resin was sucked into the mold under atmospheric pressure. In the VARTM process, the distribution media provided a high permeability region in the mold cavity, which allowed the resin to quickly flow across the surface of the laminate and then wet the thickness of the laminate. Therefore, the dominant impregnation mechanism in the VARTM process was the through-thickness flow of resin. In the final step, the composite part was cured at the room temperature and then post-cured in an oven, producing the final product NC-F, and the control sample NC-P.

3.2.4 MWNT-TiO_2 paper and laser sintering

The laser sintering process for the MWNT-TiO_2 thin film was done to the paper that was a product of a pressurized filtration process. TiO_2 ceramic nanoparticles with an average size of around 300 nm were used in the paper-making process. The MWNT-TiO_2 mix was created in four stages: (1) dispersing MWNTs into water using high energy sonication; (2) dispersing ceramic nanoparticles into water by sonication; (3) mixing the two solutions together to create a uniform suspension of MWNTs and ceramic nanoparticles, and (4) infiltrating the suspension through a filter.

Laser sintering of the MWNT thin film was performed using a SPI G3.0 laser system with a wavelength of 1064 nm. This system was operated in a pulsed mode with a pulse duration of 200 ns. It is delivered and focused through a laser scan head (ScanLab, HurryScan 14) onto the surface of the MWNT-TiO_2 thin film, that is positioned by three

linear motion stages (Newport ILS 100PP) in X, Y and Z directions. The scan head has a lens with a 100-mm focal length, and the focused laser beam has a spot diameter of ≈30 μm. To avoid chemical reactions with the ambient air, argon gas was applied in the laser sintering environment during laser sintering of MWNT thin film. More details of this MWNT-TiO_2 thin film paper was presented in recently published work [29].

3.3 Results of Ex-situ Raman spectroscopy for a MWNT-composite's manufacturing processes

Quantifying the disorder and stress throughout a manufacturing process with Raman spectroscopy will be investigated to present optimization techniques for creating these novel materials. By monitoring the microstructure development with Raman, specific microstructure characteristics can be optimized. In this section, the focus will be on assessing the manufacturing process with regards to the improvement of the reinforcement capability of the nanotubes for structural applications.

3.3.1 Raman investigation of oxidation and functionalization of MWNTs

The first step of this process, oxidation, has been studied before by Osswald *et al.* with Raman spectroscopy [68]. With the D/G ratio as a good indicator for monitoring the defects on MWNT surface [68], Osswald *et al.* was able to determine the optimal con-

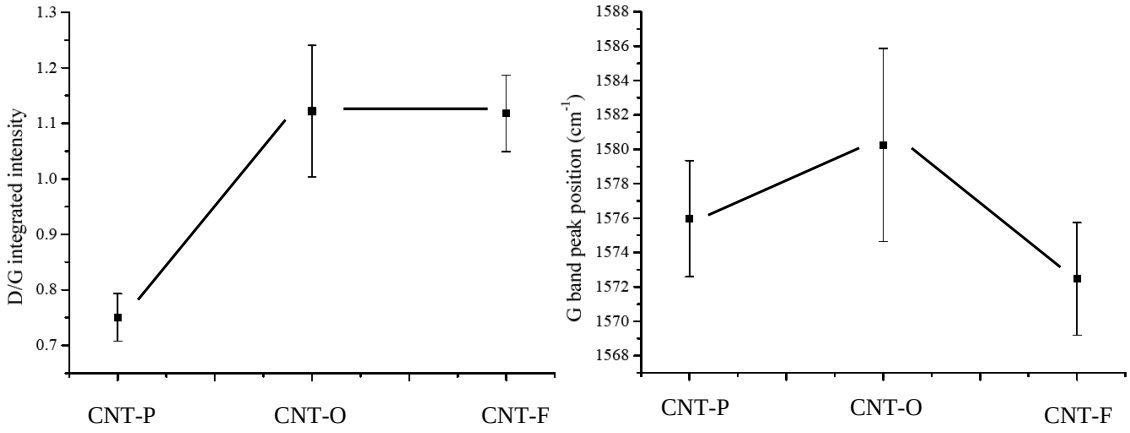

Figure 3.2: The D/G ratio (a) and the G peak position (b) for the intermediate samples of the functionalization process. Lines indicate the experimental trends for the ex-situ process. The error bars represent the standard deviation after sampling 10 random locations on each sample.

ditions to purify the MWNTs without damaging them, which can be a concern in the oxidation process [67]. Here the oxidation process was an acid treatment which not only removes amorphous carbon, but also introduces defects along the MWNT surface [96].

The D/G ratio increased between samples CNT-P and CNT-O, indicating the effects from acid treatment in Fig 3.2a. To optimize the oxidation process with Raman spectroscopy, disorders between -COOH groups and amorphous carbon need to be quantified separately. Currently, the D/G ratio represents a combination of both types of disorders, and can only quantify the amount of disorder in general. Section 2.4.5 discusses alternative fitting procedures where sub-bands could give a way to distinguish the two different origins of disorders with Raman spectroscopy.

The following steps of the functionalization process were to graft POSS using $SOCl_2$ as a precursor. The D/G ratio did not change during this functionalization process from CNT-O to CNT-F as shown in Fig 3.2a. The POSS molecules did not increase the defect concetration on the MWNTs because they bonded to -COOH functional groups that were are introduced on the MWNT surface during the oxidation process. This could enhance mechanical properties, by changing surface properties of the MWNTs, such as roughness and improving interface with the matrix. Large amounts of stress could transmit between fiber and matrix via functional groups i.e. surface defects.

The results show the G peak position had an up-shift and then a down-shift for the oxidation and grafting process respectively. Depicted in Fig. 3.2b, the uncertainty for peak position from sample to sample is of similar order to the observed peak shifts, due to the large inhomegenity in each sample . This large uncertainty relative to any changes from functionalization has been reported before [68]. It remains unclear if the observed peak position shift are induced by a increased load transfer or a electronic charging of MWNTs. Because of the large inhomegenity, the G band peak shifts could have other origins besides stress, such as a down-shift from the creation of sp^3 bonds [25] or an up-shift and down-shift could be correlated with acceptor or donor dopants respectively [78].

3.3.2 Raman investigation of pressurized filtration and resin infusion of MWNTs and MWNT papers

This process was compared between a control variable constituent of as-received pristine tubes, and functionalized tubes. This process converts the MWNT particles (CNT) into the final product (NC). The D/G ratio increased for both the pristine and functionalized tubes as seen in Fig. 3.4a. A large decrease in D/G ratio was observed for Paper-P with respect to Paper-F. This was indicative of the POSS molecules preventing an increased defect concentration. The as-received MWNTs in Paper-P contained residual metal catalysts and amorphous carbon, which unlike the POSS molecules, damaged the MWNT structure when subjected to high hydrostatic pressure.

For the pressurized filtration process, the G peak position behaved similar between both pristine and functionalized MWNTs, up-shifting more 10 cm^{-1}. Up-shifting has been reported in literature to be attributed to hydrostatic pressure [108, 60]. The MWNTs were compressed and increased to a higher density, thus this up-shift seemed to be clearly due to hydrostatic pressure. Optimizing the pressurized filtration process for mechanical properties would require a large up-shift in G band peak position (high hydrostatic pressure). This would indicate a higher density of reinforcing fibers and pre-loading. However a high density should not be substituted for an increase in disorder, and thus a minimum D/G ratio should be maintained.

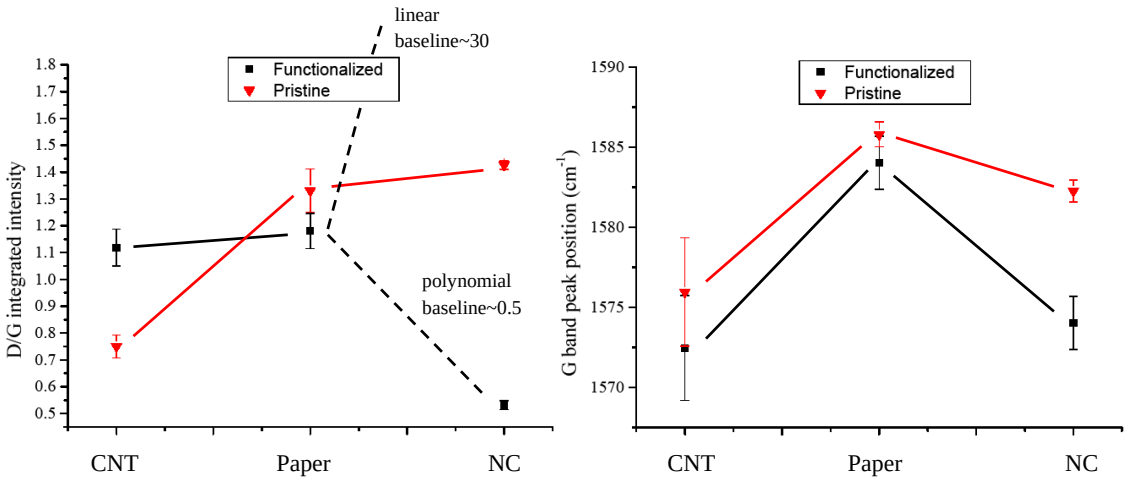

Figure 3.3: the D/G ratio (a) and the G peak position(b) for the pressurized filtration and resin infusion processes. The two dotted lines represent the two different interpretations for deconvoluting NC-F Raman spectra (sect. 3.3.2).

The G peak position down-shifted for both resin infused samples, with the NC-F obtaining a larger down-shift in Fig 3.3b. As the resin is being infused, it is proposed that the resin is pulling and stretching the MWNTs and their functional groups. This pulling behavior was similar to a uni-axial strain [51, 28], during which observes a downshift in G peak position is observed. This downshift was attributed to an increase in load transfer of the MWNTs, and the larger downshift for the functionalized sample represents a greater degree of compatibility with the host resin through improved interface properties.

The proposed mechanism for the downshifting of the G band was illustrated in Fig. 3.4. It was attributed to a combination of the drawing of the resin during the VARTM process discussed in Section 3.2.3, and a coefficient of thermal expansion mismatch between the resin and MWNTs [113]. Optimizing the resin infusion process for enhanced

mechanical properties, would require obtaining a maximum stretching of the MWNTs, which would be measured by the magnitude of the G-band downshift while maintaining a minimum D/G ratio. The stretching of CNTs during a manufacturing process has been attributed to enhanced mechanical and electrical properties [109].

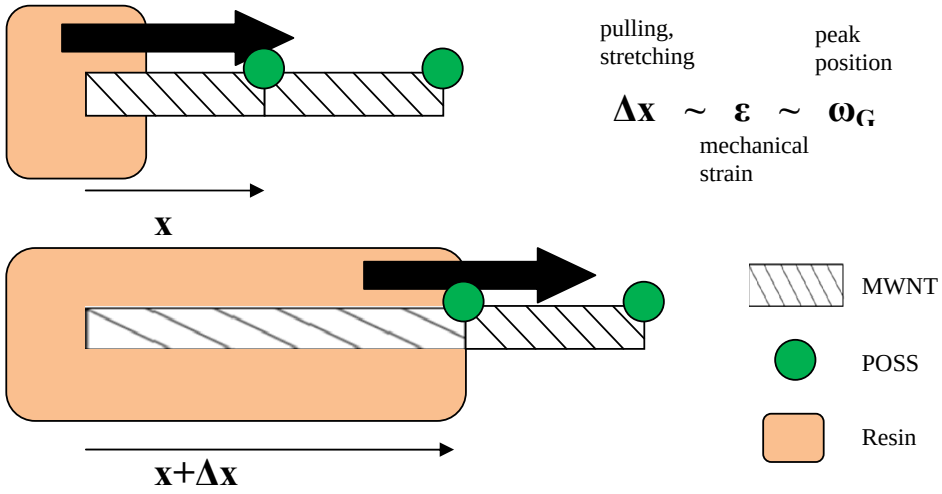

Figure 3.4: schematic of the downshifting mechanism of the G band, caused by a pulling or stretching of the MWNT by resin infusion.

The resin infusion process produced distinct differences in the Raman spectrum between the functionalized and pristine tube samples. Differences were so great, that previous deconvolution techniques were not sufficient in resolving Raman characteristics. the NC-F and NC-P spectra in Fig. 3.5c and d. The G and D doublet of the NC-F spectra had very low intensity, ≈1/150 of the NC-P intensity. Improving intensity may be achieved using a different laser excitation wavelength that is closer to the modified microstructures optical transition energy. To extract accurate D/G ratios and peak po-

sitions from this unconventional D and G doublet, a novel deconvolution procedure was used for interpreting the NC-F Raman spectra.

The NC-F spectrum was interpreted here in two ways, using a linear (Fig. 3.5e), or 3rd order polynomial (Fig. 3.5f) for baseline removal. All other conventional G and G doublets were deconvoluted with a linear baseline. However with NC-F, the linear baseline caused the D and G doublet to lose its shape, with extreme broadening of D, which yielded a D/G ratio to be approximately 30. This ratio was extremely large compared to other spectra of conventional D and G doublet shape, by over an order of magnitude. With the linear baseline producing such a large D/G ratio, an alternative baseline fit of the spectrum was used. The baseline was removed with a 3rd order polynomial that resulted in a more doublet-like appearance, with the D/G ratio being 0.5 (Fig. 3.5e), more comparable samples studied earlier in the manufacturing process.

The most important evidence that supports the use of the 3rd order polynomial baseline is the smaller D/G ratio from NC-P to NC-F. The control sample for the final product underwent resin infusion with pristine MWNTs resulting in the damaging of these unfunctionalized MWNTs during this process. The resin infusion for the NC-F sample had functional groups on the MWNT that the resin bonded to, preventing the resin from directly interacting with the MWNT structure. The decrease in the D/G ratio actually supports evidence that the resin infusion continued to remove defects in the nanotubes, possibly correcting tube-tube defects from the pressurized filtration process or diffusing any left over amorphous carbon into the resin matrix. The D/G ratio across this process

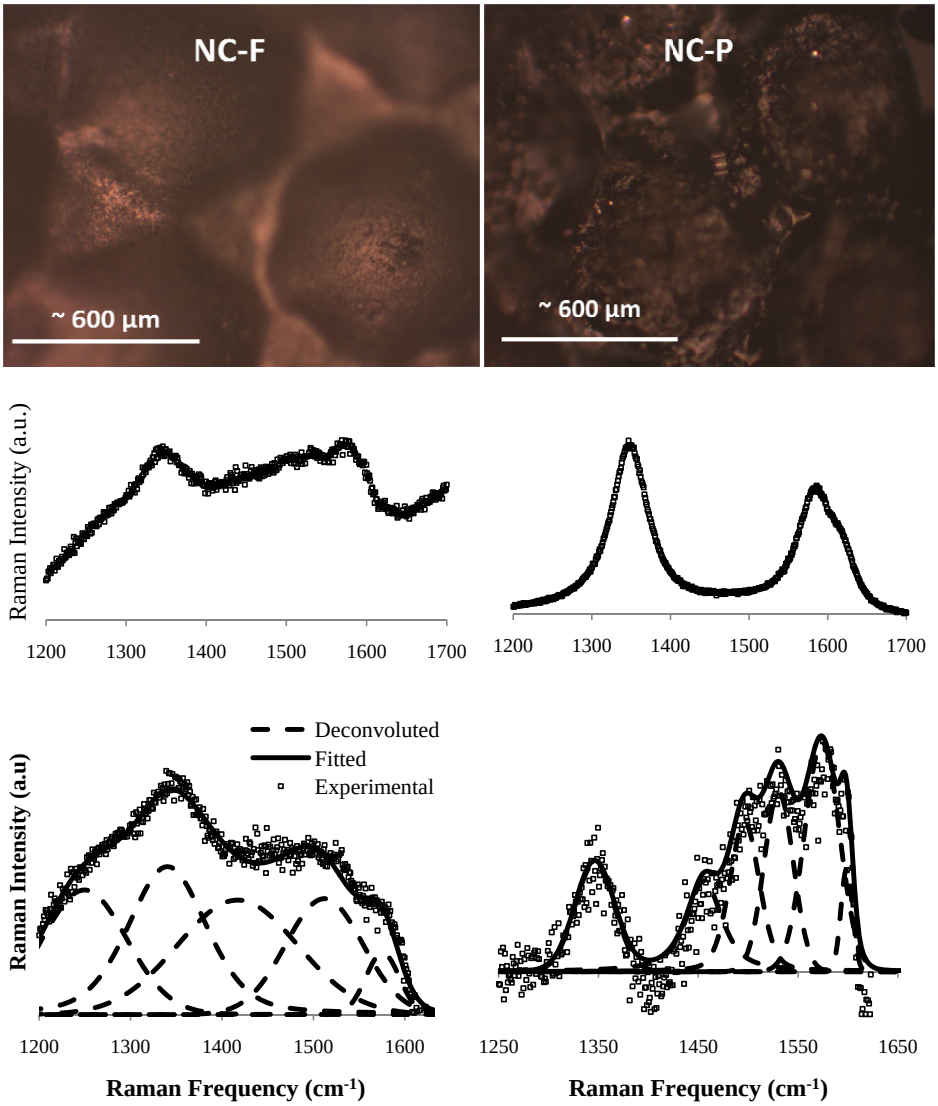

Figure 3.5: A microscope image of the NC-F (a) and NC-P (b) samples. Experimental Raman spectra for NC-F (c) and NC-P (d) samples. Different deconvolution processes utilized for interpreting the NC-F Raman spectra using a linear (e) and a polynomial (f) baseline.

for both samples was presented in Fig. 3.3a. By investigation of microscope images in Fig. 3.5a and b, The NC-F sample appears to have a much smoother and homogeneous surface than the control sample, NC-P. This was additional evidence that supports NC-F was best fit with the polynomial.

No Raman bands of the resin were observed in the NC-P spectrum within the G and D doublet frequency range. The prior statement also suggests that the NC-F spectrum's sub-bands within the G and D doublet are not of resin origin. Sub-bands in this region have been noticed before from the ends of nanotubes [35], and these ends of CNTs are places of increased heterogeneous electron transfer [76]. With the NC-F samples being more electrically conductive than NC-P, these sub-bands support the notion of an increased amount of sites for heterogeneous electron transfer. Studies on doped CNTs [78] also contained similar low frequency modes that were attributed to donor dopants. The identification and classification of these unidentified sub-bands, deconvoluted in Fig. 3.5f, will be the basis of future work to better understand the fiber-matrix electronic interaction.

3.4 Optimizing laser sintering parameters with Raman spectroscopy

Laser sintering melts the TiO_2 nanoparticles and encapsulates them around the MWNT structure. The goal for this section was to use Raman spectroscopy to find the optimum laser sintering parameters that would achieve maximum bonding of the encap-

sulating TiO_2 particles to MWNT structure, while simultaneously, not damaging the MWNT structure. Before the sintering parameters were optimized, the Raman spectra was checked to verify the integrity of MWNT structure. The presence of intact MWNT structures were supported by the intensity increase of the G band with respect to D from unsintered to sintered samples. The G band is an intrinsic features of the MWNT, while the D band is a disorder induced phonon [20].

Two sintering parameters of laser fluence(J/cm^2) and scanning speed (mm/s) were to be optimized. Using similar Raman characteristics as the *ex-situ* manufacturing process, D/G ratio and G band peak position were of primary focus because they represent defect concentration in MWNT surface, and strain in the C-C bonds respectively. Therefore, to optimize fluence and scanning speed, D/G ratio was desired to be a minimum, while the down-shifting of the G band peak position was to be maximum.

By investigation of Fig. 3.6b, the D/G ratio's dependence on scanning speed was dependent on the fluence of the laser. For most fluences, the D/G ratio was positively correlated with increased scanning speed. For an intermediate fluence of 2.2 J/cm^2, the D/G ratio was negatively correlated with scanning speed. This negative correlation was desirable, because this indicated the capability of the laser light to selectively remove amorphous carbon or impurities from the material and has been observed in laser sintered photocatalytic coatings [14]. Unfortunately, a global minimum was not present in this experimental trial, but results here suggest that the optimum scanning speed will be greater that 150 mm/s, outside of the scanning speed regime studied here. Fig. 3.6a was

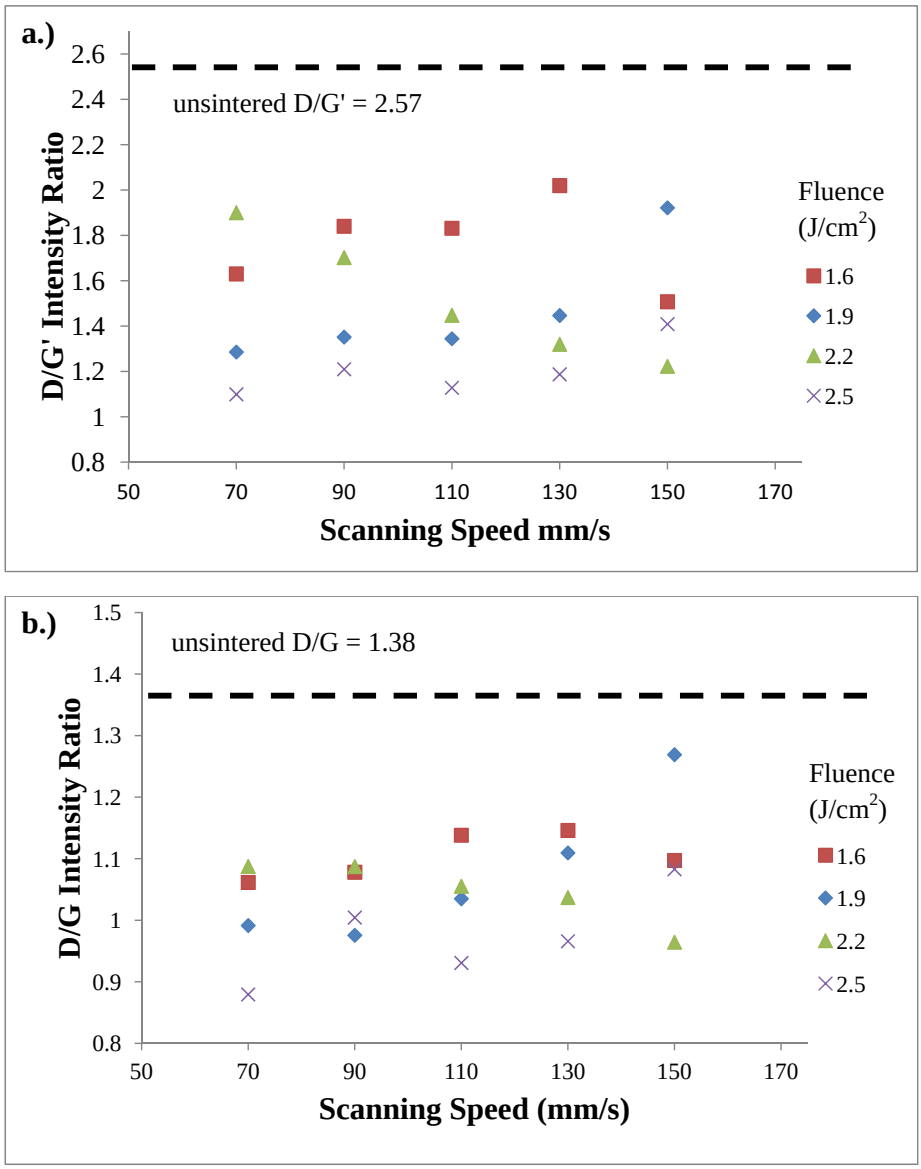

Figure 3.6: Raman I(D/G) values for laser sintering process parameters. The dotted lines represent the unsintered spectral parameters for I(D/G)

an instance where the G' band intensity was more sensitive to the laser sintering effects than D. The G' band is intrinsic to the MWNT structure [22], and a higher intensity would be correlated with a higher purity. Its relationship with scanning speed and laser fluence was the same as the D/G ratio, only more pronounced.

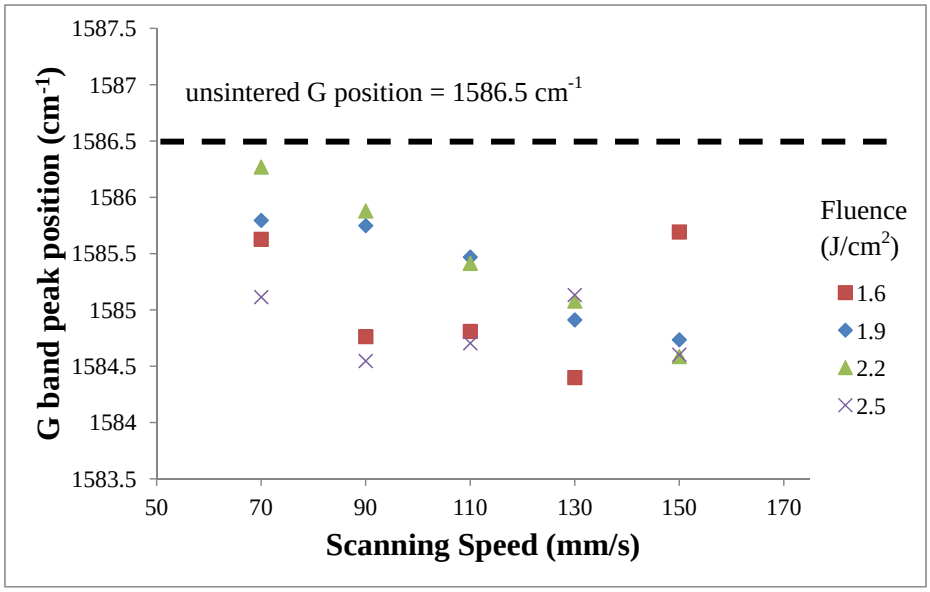

Figure 3.7: Raman G band position values for laser sintering process parameters. The dotted lines represent the unsintered spectral parameters for G band position.

The G peak position was investigated in a somewhat detailed fashion for this sintering process to understand the molecular strains taking place in the MWNT structure during this process. When the TiO_2 particle is melted and encapsulates the MWNT structure, the molten TiO_2 structure also agglomerates with neighboring particles. This agglomeration induces a movement of the particles, that stretches the MWNTs. This

stretching of the MWNTs is desirable, and is indicative through a down-shift of the G peak position, similar to uni-axial strain [51, 28].

Fig 3.7 has G peak position data for the sintering parameters of fluence and scanning speed. The down-shifting relationship with scanning speed was consistent with intermediate laser fluences of 2.2 and 1.9 J/cm^2. This consistent G band relationship is desirable and agrees with the D/G relationship; that the optimum scanning speed is above 150 mm/s for a fluence of 2.2 J/cm^2. However the sporadic relationship with peak position and scanning speed for the maximum and minimum laser fluences of 2.5 and 1.6 J/cm^2 respectively, do not have a consistent relationship. This sporadic relationship is proposed to be the result of an inconsistent pulling behavior that is caused by the viscosity of the molten particles. The intermediate fluences melts the TiO_2 particles to an appropriate temperature where the viscosity of the molten TiO_2 particle is compatible with the surface of the MWNT structure.

3.5 Concluding remarks

The results from the ex-situ data shows that the optimization of an entire manufacturing process can be achieved by isolating processing parameters and testing their influences on the Raman spectrum. Results presented in this section, were conducted with a single laser excitation, however similar experiments in the future will include variable excitation Raman spectroscopy. The same technique used in this section with additional excitation

energies could unveil how the different CNT species (diameter and chirality combinations) will behave under resonance conditions. The next chapter will explore the benefits of using variable Raman excitation

CHAPTER 4
MULTIPLE WAVELENGTH SPECTROSCOPY TO CHARACTERIZE CNT STRUCTURES

The double resonance Raman (DRR) phenomenon has been used to explain results obtained *via* multiple wavelength spectroscopy from many different types of carbon based materials [24]. The origin of this phenomenon and the benefits for characterizing microstructure using multiple wavelength spectroscopy will be investigated. This section will investigate and compare results obtained here from the DRR experimental data obtained before and after the pressurized filtration process of the MWNT-composite discussed in Section 3.2.2.

4.1 Introduction

The electronic transition energies for SWNT structure is so sensitive that it allows for specific identification of (n,m) indices's by tuning laser excitation energy [42, 27]. This extremely sensitive Raman cross section for SWNTs, is produced from a strong coupling that occurs between the electrons and phonons in the quasi 1-D CNTs [20]. Raman scattering for carbons is a resonant process. Therefore, a CNT whose resonant electronic transition energy (E_{ii}) matches the excitation energy will be preferentially excited [24, 41].

The Raman process is not so sensitive for MWNTs because of the large number of discrete geometries that can exist for the larger CNT diameters as discussed in Section

1.2. For MWNTs, the Raman cross section is reduced from a decreasing 1-D character of the larger outer walls [44]. For these reasons the Raman spectrum from MWNTs is easily comparable to graphite and disordered carbon [6].

For the DRR effects, literature has reported results that could tie a connection between the multiple phases of carbon nanostructures. Comparing DRR experimental results, it has been shown that SWNTs [80] could behave similar to graphite [24]. Interestingly, a similar study showed that the purification of MWNTs [48] behaved differently from defect healing reported for SWNTs [80] and graphite [24]. This comparison suggests that MWNTs could exhibit unique properties that do not exist in either graphite or SWNTs.

4.1.1 Background in double resonance Raman spectroscopy

A physical explanation of the DRR effect is associated with elastic phonons scattering close to the K and Γ point of the graphite Brillouin zone [1, 85, 86, 101]. If any Raman characteristic is dependent on the laser excitation, it could be due to a DRR effect [26]. It has been an area of recent research to relate the DRR phenomenon to disorder for SWNTs [80], MWNTs [48, 93], and other carbons [24, 111]. These findings are not always consistent because of the wide array of carbon materials and origin of defects in these studies. The most popular DRR features for the CNTs is the D band, where the intensity and peak position are very sensitive to laser excitation energy [71, 58]. The D band is

also associated with a scattering event involving a π electron [80]. With the D bands intensity increasing significantly at lower excitation energies, the π bond obtains a better resonance condition. Alternatively, when excitation energies are higher, the probability for the scattering event to involve a σ electron is 250-300 times larger [111, 25]. This coincides with a very intense G band in the Raman spectrum for excitation approaching ultraviolet (UV) with a resonance condition favoring the σ bond.

4.2 Multiple wavelength spectroscopy experiment

Samples consisted of MWNTs received from Nanolabs, which were approximately 20nm diameter and 10 μm in length. The two samples studied were extracted from an intermediate phase of a manufacturing process of a multi-functional MWNT-polymer nanocomposite [54]. The two samples, CNT and Paper, represent the sample before and after the pressurized filtration process respectively as discussed in Section 3.2.2. SEM images were taken of the CNT and Paper sample in Fig. 4.1.

An InVia Raman Microscope was used to study the CNT-composite with multiple laser excitations (633, 514, 442, and 325nm). The laser dot size for this experiment was $\approx 1\ \mu m^2$ with a 50x objective. All laser excitations were calibrated with a Silicon peak of 520 cm^{-1} before measurements. The excitation of 325 nm required the longest exposure time of 300 sec because its laser power was only 1 mW. Laser powers used for 422, 514, and 633 nm excitation were 10, 9.5, and 12.5 mW respectively. Thus,

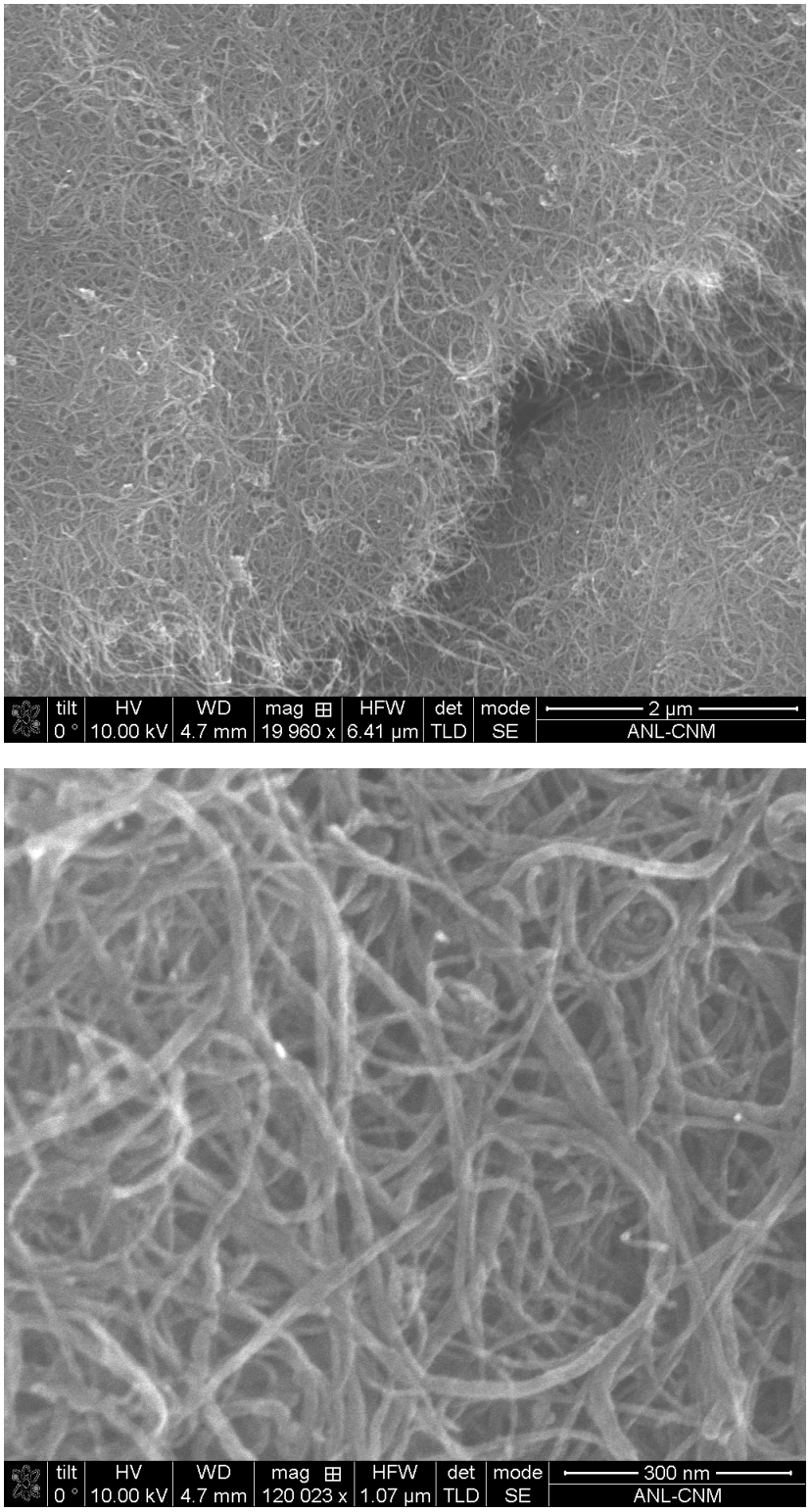

Figure 4.1: SEM images of the MWNT thin film after pressurized filtration (Paper)

accumulation times for these visible excitations were relatively short (30 seconds). The sample was visually checked to ensure there was no thermal damage from laser heating. Multiple measurements were taken at random locations of both samples for all laser excitation energies and the variation in data is represented by error bars for the figures in the results section.

A deconvolution method using 5 PV functions, discussed in Section 2.3.2, was used to evaluate the results of the G and D doublet. 5 peaks were assigned as the T band 1200 cm^{-1}, D band 1380 cm^{-1}, A band 1480 cm^{-1}, G band 1590 cm^{-1}, and D' band 1610 cm^{-1}. This 5 PV peak assignment is valid for the visible excitation used. However for the UV excitation, the G and D doublet was only fitted with D, A, and G bands because of a different G and D doublet shape in Fig. 4.2. Here, DRR effects are reported for D, G and D' bands with reference to excitation energy (eV).

Several spectral characteristics were monitored including peak position (ω), full width half max (FWHM, γ), and the D/G integrated intensity ratio. These characteristics were monitored for every laser excitation and differences between these characteristics, before and after the pressurized filtration process, will henceforth be preceded with a δ. For example, the change in G band peak position ($Paper(\omega_G) - Pristine(\omega_G)$) for this process will be refereed to as $\delta\omega_G$, and a different value will exist for every excitation energy.

The DRR effects were also investigated and the relationship of a Raman characteristic with excitation energy will be preceded by a Δ. For example, the DRR effect for the D band peak position would be referred to as $\Delta\omega_D$ which commonly has a linear slope

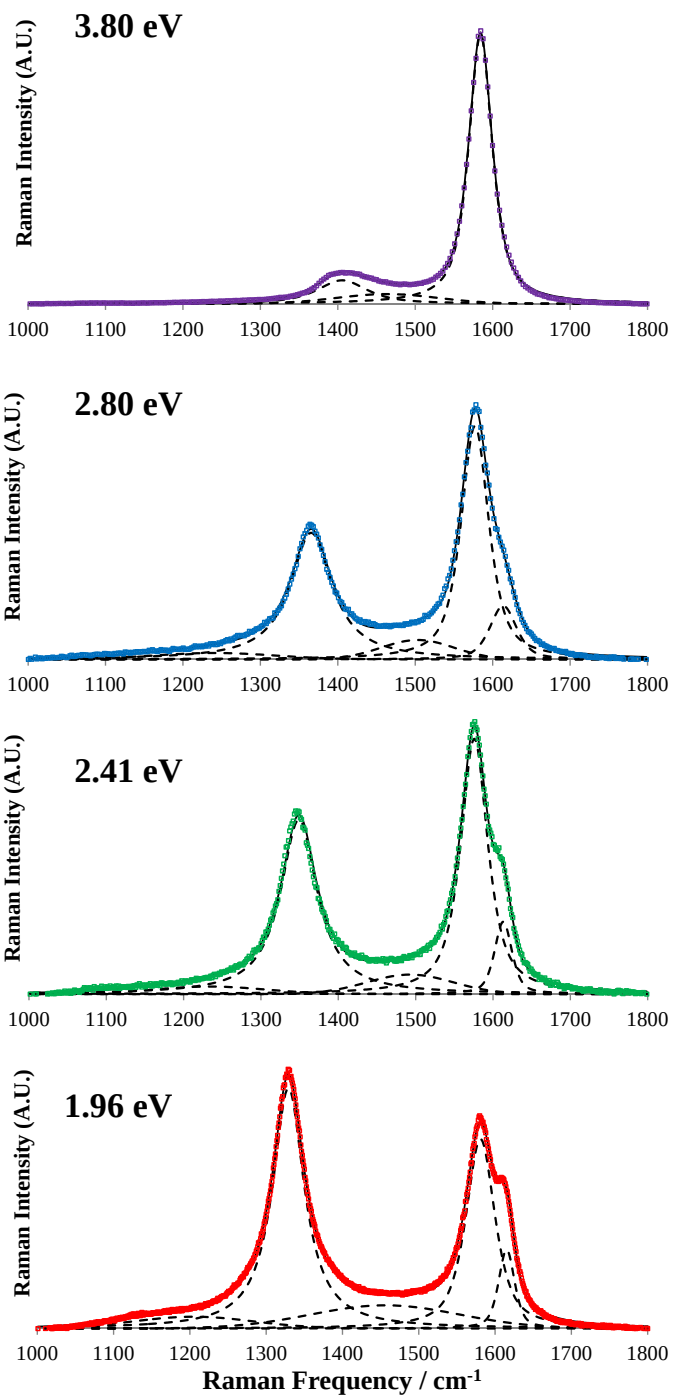

Figure 4.2: The Raman spectrum for each of the different excitation energies of 3.8(a.), 2.8(b.), 2.41(c.), and 1.96(d.) eV respectively.

of 50 cm^{-1}/eV for most carbon based materials [86]. While DDR effects have been investigated as linear functions [48, 69], recent studies have assigned them as higher order functions [93]. Some results here will be referring to the DRR process as linear, but some of the experimental results for the pressurized filtration process suggest they are of a higher order. For DRR processes that produce linear relationships between excitation energy and the Raman characteristic, slopes are considered here to be quenched or enhanced if it approaches zero or increases in magnitude respectively. A DRR process for higher order functions could also be considered to be quenched if there is a reduction in the magnitude of the higher order coefficients, resulting in less pronounced maxima and minima.

4.3 Experimental Results from Multiple Wavelength Spectroscopy for a pressurized filtration process

4.3.1 Peak positions results

The $\Delta\omega_D$ was observed to be enhanced for the pressurized filtration process in Fig. 4.3a. Literature reports that an enhancement of this feature is attributed to defect healing in SWNTs [80], the graphitization of hydrogenated tetrahedral amorphous carbon (ta-C:H) [24], and from lack of defects when comparing SWNTs and MWNTs [69]. Here, a quenching of the maxima and minima in the $\Delta\omega_D$ function was observed. By inspection of

experimental data by Ferrari *et al.* [24], a better linear correlation (R^2) could be observed in the DRR process for the graphitization of ta-C:H at higher annealing temperatures, which is the equivalent of a quenching of second and third order features.

The D band revealed that the there were no healing affects intrinsic to the pressurized filtration process. However, an increased linear correlation was observed for $\Delta\omega_D$ was similar to a graphitization process. This indicates that a mild organization and condensation of the MWNTs assembles the microstructure, similar to that of a graphitization process. This suggests that the linear correlation of $\Delta\omega_D$ could potentially optimize the assembly of the microstructure for the pressurized filtration process

The G band peak position normally does not disperse with SWNTs [94], but sometimes it disperses linearly with low R^2 values for MWNTs [48] or even with high R^2 values for disordered carbons [24]. MWNTs have been reported to possess DRR features in a study by Lee *et al.*, where $\Delta\omega_G$ was quenched from defect healing during a plasma oxidation process [48]. Before pressurized flitration, ω_G for the DRR process was not observed to be linear, but dynamic with pronounced local maxima and minima with respect to laser excitation energy. After the pressurized filtration process, the local minimia and maxima disappeared for$\Delta\omega_G$, as the G band converged to 1577 cm^{-1} for visible excitations in 4.3b.

The ω_G was also investigated *per* excitation and an up-shift only occurred for higher excitation energies of 3.8 and 2.8 eV, while down-shifts occurred for lower excitations of 2.41 and 1.96 eV. This observation of up-shifts and down-shifts suggest that the

competition between DRR effects and C-C stretching modes are taking place [26]. The hydrostatic pressure effects are only observed for the higher laser excitation energies. This suggests that by using the higher excitation energies, the DRR effects are outweighed by the effects of hydrostatic pressure.

Here, the G band was observed to be affected by some DRR effects, with a shifting of peak position that can not be explained by C-C force constants for the pressurized filtration process. Filho *et al.* concluded that the DRR process can overcome the C-C force constants when there is a large distribution of CNT diameters [26] and a higher density of MWNTs would create a higher diameter distribution for the pressurized filtration process. Thus, the convergence of the peak position for visible excitation of the Paper sample could be the cause of a DRR that was enhanced with the increased density of MWNTs. However, this convergence did not continue for the highest excitation energy used here of 3.8 eV, which showed C-C force constants that are consistent with the hydrostatic pressure effects that are intrinsic to the pressurized filtration process.

From the G band peak position, it was observed that the DRR process was enhanced by the pressurized filtration process, and could affect microstructural strain measurements. However, the C-C force constants could outweigh the DRR effects if the excitation energy is high enough. The D' band position ($\omega_{D'}$) behaved very similar to the G band, where the $\delta\omega_{D'}$ values were positive and negative for higher and lower excitation energies respectively, converging the peak position to an average of about 1612 cm^{-1}/eV.

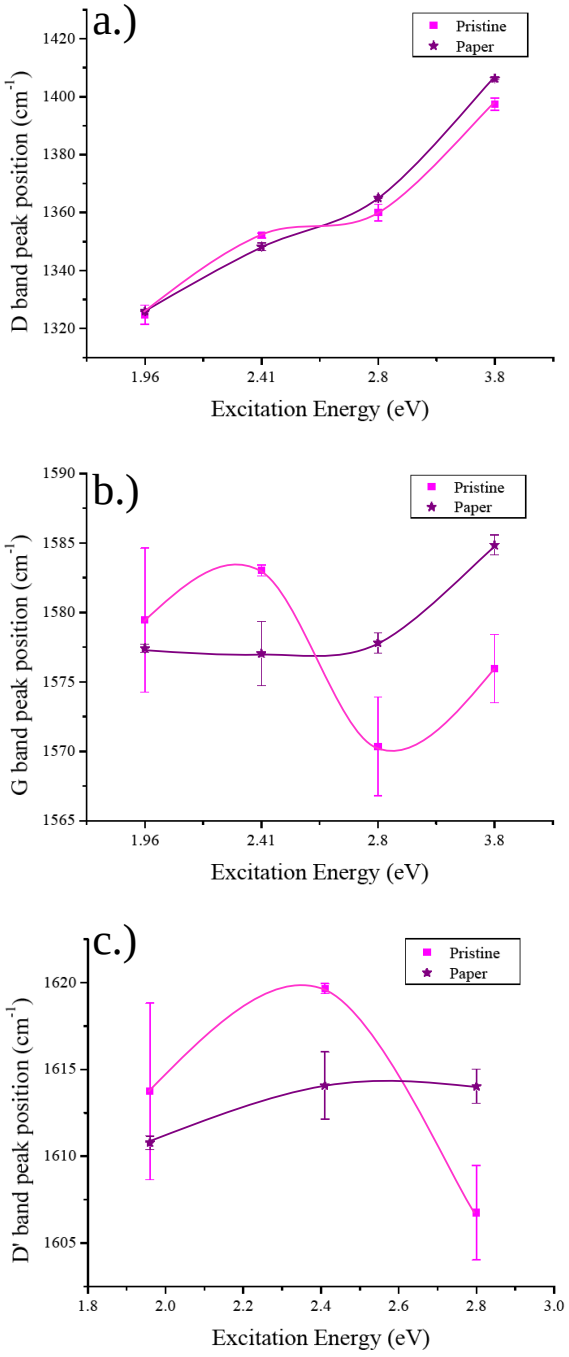

Figure 4.3: Peak positions for D (a.), G (b.), and D' (c.) bands before and after pressurized filtration for all excitation energies. Polynomial curves were used to help guide the eye.

4.3.2 Full width half max results

Narrow line-widths have been found to be good indicators of structural order [2]. Here, the $\delta\gamma$ values for all bands and excitations were consistently negative, indicating the pressurized filtration process increased order. When linear functions were used, $\Delta\gamma_G$ and $\Delta\gamma_{D'}$ were quenched, while $\Delta\gamma_D$ did not change significantly in Fig. 4.4.

Lee *et al*. had results that agreed with the sign of linear slope values for $\Delta\gamma_D$ reported here. However, the difference in fitting procedure does make it difficult to compare γ_D as discussed in Section 2.4.4. For the pressurized filtration process, no significant change in slope was noticed when a linear function was fit to $\Delta\gamma_D$,

In this study, $\Delta\gamma_G$ was negative, which is different than a study by Lee *et al*. [48] who found $\Delta\gamma_G$ to be positive for MWNTs. This disagreement may be partly due to the difference in fitting, where Lee *et al*. used the "standard" fit and here a 5 PV fit was used, as discussed in Chapter 2. A study by Ferrari and Robertson found $\Delta\gamma_G$ to be quenched with the graphitization of ta-C:H under higher annealing temperatures [24]. A very similar effect was noticed here, providing additional evidence that the pressurized filtration process organized the microstructure to some degree, similar to a graphitization process.

No results were available to compare $\Delta\gamma_{D'}$ values because Lee *et al*. used the standard fit which produced a negative linear slope. Here, the 5 PV fit produced a positive linear

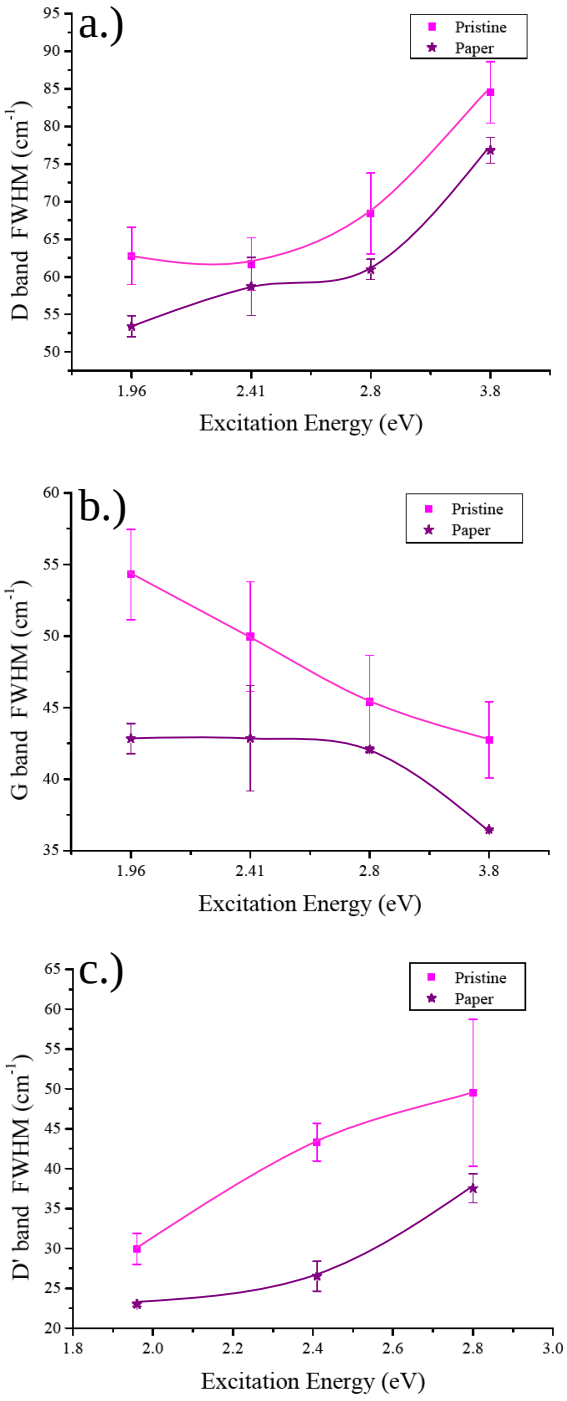

Figure 4.4: Peak widths for D (a.), G (b.), and D' (c.) bands before and after pressurized filtration for all excitation energies. Polynomial curves were used to help guide the eye.

slope. For the pressurized filtration process, a linear fit to $\Delta\gamma_{D'}$ was quenched. Here, $\Delta\gamma_D$ and $\Delta\gamma_{D'}$ were of the same sign, narrowing with decreasing excitation energy.

4.3.3 D/G ratio

$\Delta(D/G)$, representing the function of integrated intensities with respect to laser excitation, has been reported to be quenched when there was minimal disorder [2, 80, 69]. However this is contrary to other studies that report an enhanced $\Delta(D/G)$ with minimal disorder [48, 24]. From comparing these contradictions in literature, it can be assessed that the $\Delta(D/G)$ depends not only on the carbon species (graphite vs. SWNTs), but also depends on the type of disorder within a certain species of carbon, indicated by the discrepancies for the relationship of $\Delta(D/G)$ and disorder for MWNT studies [2, 48].

Here, the DRR process underwent little change after the pressurized filtration process in Fig. 4.5. $\Delta(D/G)$ ratio values are much more sensitive to purification effects in MWNTs [48] when compared to defects intrinsic to the pressurized filtration process. The D/G ratio increased almost equally *per* laser excitation energy, suggesting that the defects intrinsic to changing $\Delta(D/G)$ values are different from those that change $\delta(D/G)$.

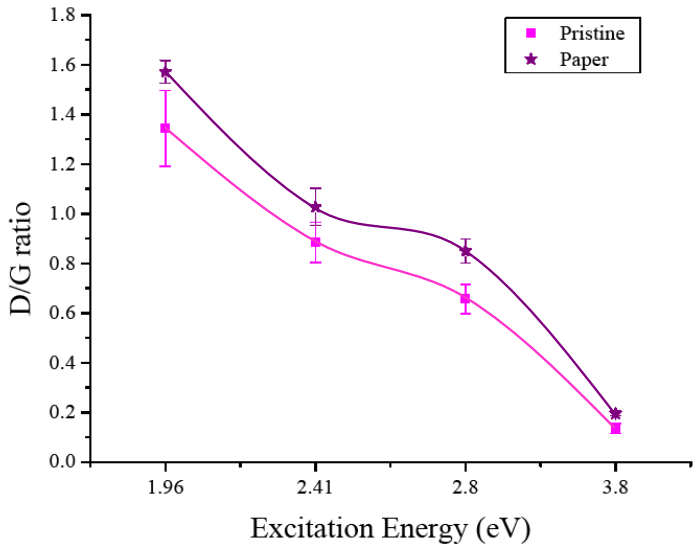

Figure 4.5: The D/G ratio before and after pressurized filtration for all laser excitation energies. Polynomial curves were used to help guide the eye.

4.4 Discussion

A narrowing of Raman bands could indicate increased resonant conditions [39]. The $\Delta\gamma_G$ value was negative, indicating a narrowing of the G band with increasing excitation energy. This further emphasizes the relationship between the σ bond and the C-C stretching modes probed with higher efficiency for higher excitation energies [111]. This increased resonance with the σ bond, made the stress sensitive character of ω_G quench the DRR effects.

The $\Delta\gamma_D$ and $\Delta\gamma_{D'}$ values were both positive supporting the notion that the π bonds are represented by the D band [1]. The defects that are intrinsic to $\Delta\gamma_D$ and $\Delta(D/G)$ were mildly affected by the pressurized filtration process. These characteristics, intrinsic

to a scattering event with the π bond [1], suggest that they are better for characterizing chemical defects on CNTs, which are not taking place in the pressurized filtration process. The $\Delta\omega_{D'}$ behaved very similar to $\Delta\omega_G$, suggesting that this band is a hybrid combination of π and σ bond features.

These resonance conditions that select the σ and π bonds are illustrated with Fig. 4.6. The higher energy excitation could be capable of penetrating deeper into the Brillouin zone, and interacting with electrons closer to the σ bond. Then, if an excitation has a lower energy, then the interactions with the photon and electron take place at the outer edges of the Brillouin zone, near the π bond.

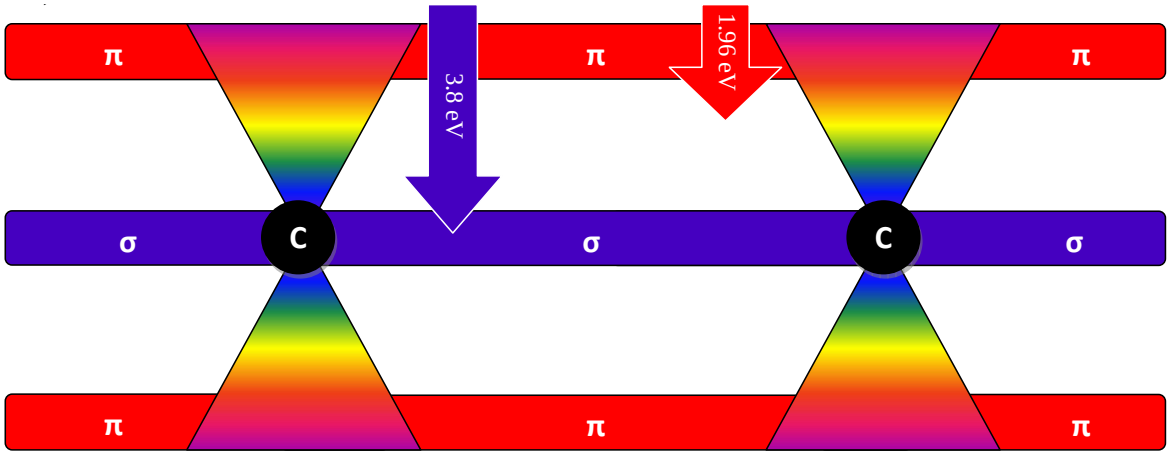

Figure 4.6: Illustration of the connection between laser excitation energy and probing the atomic structure of CNT structure

4.5 Conclusion

Here, it was shown that some DRR features for the pressurized filtration process were very similar to graphitization effects of ta-C:H [24]. This indicates that the pressurized filtration process condenses the microstructure, mildly organizing it, as if it were assembling an intricate network of MWNTs. This suggests, that the DRR process could be used to obtain more detailed microstructural information, than conventional Raman techniques with a single excitation. The ability to probe σ and π bonds with higher and lower excitation energies respectively, could help distinguish disorders related to either the σ or π bonds.

CHAPTER 5
CONCLUSIONS

5.1 Summary of results

The results of this work show that optimization for a wide range of manufacturing process for CNT composites is available with Raman spectroscopy. a precise and consistent deconvolution of the Raman spectra was of first priority. A fitting procedure utilizing pseudo-Voigt functions was successful in minimizing uncertainty with a 5 peak fit. The Raman characteristics of primary interest were the G band peak position (ω_G) and D/G integrated intensity ratio (D/G). This study proved that the 5 PV peak assignment minimized the uncertainty with respect to the "standard" fit, used by many researchers for MWNTs and their composites, by $\approx$ 65 and $\approx$ 46 % for ω_G and D/G respectively. Here, a consistent and organized representation of the G and D doublet was presented that should be applied to all future work for CNTs with applicable G and D doublets.

A concurrent study was taking place with the *ex-situ* study of a manufacturing process of a polymer-MWNT composite. The evolution of the G and D doublet was monitored, and reflected intrinsic microstructural changes for each stage in manufacturing. By correlating the Raman characteristics with structural properties, It was possible to present optimization techniques for oxidation, functionalization, pressurized filtration, and resin infusion.

The Raman characteristics gives insight to the physical mechanism that is intrinsic to each manufacturing process. Understanding the Raman relationships to physical mechanisms of CNTs, allows for optimization of manufacturing parameters by controlling the Raman characteristics. Optimizing the purification process with minimizing the D/G ratio has been well established in literature [67, 68, 7]. The physical mechanisms behind the functionalization process can be numerous with the approach taken to functionalize the CNTs [84, 95]. Here, it was concluded that correlating the physical mechanisms behind a functionalization process is of high priority for future studies, and an area being investigated by a few different research groups [63, 96, 64]. The G band is sensitive the electrical charges by an electrode potential [118] or dopants [78], and should be the Raman characteristic of interest in future experiments which attempt to optimize a functionalization process.

Here, optimization techniques were presented, for the first time, for pressurized filtration, resin infusion processes, and laser sintering processes. Optimizing both processes were proposed by maximizing the magnitude of the stress sensitive G band shifts, while keeping the disorder induced D/G ratio to a minimum. The direction of the G band shift determined the physical mechanism that was intrinsic to each process, and led to a better understanding of what the CNT structure was experiencing. These same optimization principles were applied to a laser sintering process, where laser sintering parameters of fluence and scanning speed were optimized by maximizing the magnitude of the G band shift and minimizing the D/G ratio.

The goal of Chapter 4 was to see what kind of additional information on the microstructure could be obtained, and what kind of resonance effects would affect the Raman spectrum when the excitation energy was changed. Results from the multiple wavelength Raman spectroscopy suggest that some stress sensing Raman characteristics may be masked at lower excitation energies by the DRR phenomenon. It was reviewed that the lower excitation energies probe the π bond [2], and *vice versa*, higher excitations probe the σ bond with higher efficiencies [111]. Thus, by probing with higher excitation energies, DRR effects could be avoided, and a better measurement of the C-C force constants could be obtained.

The pressurized filtration process affected the DRR characteristics in a similar way to those reported for a graphitization process by Ferrari *et al*. [24]. Graphitization is associated with the removal of some intrinsic microstructural defects. However, The DRR effects does not suggest a large amount of defect healing associated to the pressurized filtration process when compared studies for SWNTs [80] or MWNTs [48]. Thus, it is significant to separate the origins of defects associated with the pressurized filtration process to be of similar to the graphitization process of MWNTs. DRR properties such as$\Delta\omega_D$ could be used to optimize this structural ordering of MWNTs, similar to graphitization.

5.2 Future work

5.2.1 In-situ temperature studies

Temperature relationships for peak positions (ω) are well documented Raman characteristics in literature for CNTs. Peak positions are a desirable characteristic to accurately quantify because they can help determine temperature dependent force constants for the C-C stretching modes, particularly for the G-band [81]. This makes resolving accurate peak positions of higher priority.

Temperature dependent G band peak position, ω_G, has been a tool to characterize Young's modulus [55] and residual stress within CNT nano-composites [32, 105] using thermal mismatch strains of the matrix-fiber interface [33]. In these prior works, a change of $\Delta\omega_G$, with respect to pristine tubes prior to impregnation into a matrix, was monitored during *in-situ* temperature experiments to quantify the strain sustained by the nanotubes. At temperatures below the glass transition temperature, T_g, a hydrostatic pressure was subjected to the nanotubes [105], and the strain sustained as a function of G-band position was used to quantify the interface of different CNT precursors for CNT/epoxy composites [32].

Future work would be using these temperature relationships and finding the best chemistry to modify the interface between the matrix and the CNT-fiber. Optimizing this interface is important for enhancing CNT composites, and determining interface

properties with a small temperature experiment could be much more cost effect than creating a large bulk specimen for mechanical testing.

5.2.2 In-situ atomic force microscope studies

An atomic force microscope (AFM) is an excellent tool for CNT characterization. The accurate topography measurements achievable are ideal to calculate the diameter distribution for dispersed CNTs. AFM nano-indentation capability is capable of deriving the elastic modulus for CNT-composites [66]. This combined with correlating Raman properties will be significant the efforts to improve strength of CNT-composites.

Recent studies have shown that AFM devices are capable of measuring the friction on the surface of the nanotubes [56]. This opens up an interesting field of research that could correlate the stretching ability of CNTs to their surface friction. This surface friction could also be a variable of the functionalization technique, and allow for optimization thereof. Complementary Raman and AFM measurements could correlate mechanical properties with the Raman spectrum, and allow for a further understanding of the fundamentals of the CNT structure. This will be a subject of future investigation.

LIST OF REFERENCES

[1] E. Antunes, A. Lobo, E. Corat, and V. Trava-Airoldi. Influence of diameter in the Raman spectra of aligned multi-walled carbon nanotubes. *Carbon*, 45:913–921, 2007.

[2] E. F. Antunes, A. Lobo, E. J. Corat, and V. T.-A. et. al. Comparative study of first- and second-order Raman spectra of MWCNT at visbile and infrared laser excitation. *Carbon*, 44:2022–2211, 2006.

[3] S. Bachilo, M. Strano, C. Kittrell, R. Hauge, R. Smalley, and R. Weisman. Strucutre-assigned optical spectra of single-walled carbon nanotubes. *Science*, 298:2361, 2002.

[4] M. R. Baldan, E. C. Almeida, A. F. Azevedo, E. S. Goncalves, M. C. Rezende, and N. G. Ferreira. Raman validity for crystallite size L_a determination on reiculated vitreous carbon with different graphatization index. *Applied Surface Science*, 254:600–603, 2007.

[5] S. Berber, Y.-K. Kwon, and D. Tomanek. Unusually high thermal conductivity of carbon nanotubes. *Physical Review Letters*, 84:4613, 2000.

[6] E. Boccaleri, A. Arrais, and A. Frache. Comprehensive spectral and instrumental approaches for the easy monitoring of features and purity of diffrent carbon nanostructures for nanocomposite applications. *Materials Science and Engineering B*, 131:72–82, 2006.

[7] S. Bose, R. Khare, and P. Moldenaers. Assesing the strengths and weaknesses of various types of pre-treatments of carbon nanotubes on the properties of polymer/carbon nanotubes composites: A crtical review. *Polymer*, 51:975–993, 2010.

[8] V. Brar, G. Samsonidze, M. Dresselhaus, G. Dresselhaus, R. Saito, A. Swan, M. Unlu, B. Goldberg, A. Filho, and A. Jorio. Second-order and combination modes in graphite, single-wall carbon nanotube bundles, and isolated single-wall carbon nanotubes. *Physical Review B*, 66:155418, 2002.

[9] S. Brown, A. Jorio, and M. Dresselhaus. Observations of the D-band feature in the Raman spectra of carbon nanotubes. *Physical Review B*, 64:073403, 2001.

[10] S. D. M. Brown, P. Corio, A. Marucci, M. A. Pimenta, M. S. Dresselhaus, and G. Dresselhaus. Second-order resonant Raman spectra of single-walled carbon nanotubes. *Physical Review B*, 61:7734–7742, 2000.

[11] S. D. M. Brown, A. Jorio, P. Corio, M. S. Dresselhaus, G. Dresselhaus, R. Saito, and K. Kneipp. Origin of the Breit-Wigner-Fano lineshape of the tangential G-band feature of metallic carbon nanotubes. *Physical Review B*, 63:155414, 2001.

[12] M. Burghard. Electronic and vibrational properties of chemically modified single-wall carbon nanotubes. *Surface Science Reports*, 58:1–109, 2005.

[13] A. Carpinteri and N. Pugno. Super-bridges suspended over carbon nanotube cables. *Journal of Physics, Condensed Matter*, 20:474213, 2008.

[14] M. Castro, E. Sam, M. Veith, and P. Oliveira. Structure, wettability and photocatalytic activity of CO_2 laser sintered TiO_2-multi-walled carbon nanotube coatings. *Nanotechnology*, 19:105704, 2008.

[15] G. Chen and H. Shimizu. Multiwalled carbon nanotubes grafted with polyhedra oligomeric silsesquioxane and its dispersion in poly(l-lactide) matrix. *Polymer*, 49:943–951, 2008.

[16] S. B. Cronin, A. K. Swan, M. S. Unlu, B. B. Goldberg, M. S. Dresselhaus, and M. Tinkham. Resonant Raman spectroscopy of individual metallic and semiconducting single-wall carbon nanotubes under uniaxial strain. *Physical Review B*, 72:035425, 2005.

[17] A. Cuesta, P. Dhamelincourt, J. Laureyns, A. Martinez-Alonso, and J. M. D. Tascon. Comparative performance of X-ray diffraction and Raman microprobe techniques for the study of carbon materials. *Journal of Materials Chemistry*, 8:2875–2879, 1998.

[18] W. Ding, D. A. Dikin, X. Chen, R. D. Piner, R. S. Ruoff, E. Zussman, X. Wang, and X. Li. Mechanics of hydrogenated amorphous carbon deposits from electron-beam-induced deposition of a paraffin precursor. *Journal of Applied Physics*, 98(1):014905, 2005.

[19] S. Doorn, D. Heller, P. Barone, M. Usrey, and M. Strano. Resonant Raman excitation profiles of individually dispersed single walled carbon nanotubes in solution. *Applied Physics A*, 78:1147–1155, 2004.

[20] M. Dresselhaus, G. Dresselhaus, A. Jorio, A. S. Filho, and R. Saito. Raman spectroscopy on isolated single wall carbon nanotubes. *Carbon*, 40:2043–2061, 2002.

[21] M. Dresselhaus, G. Dresselhaus, R. Saito, and A. Jorio. Raman spectroscopy of carbon nanotubes. *Physics Reports*, 409:47–99, 2005.

[22] M. S. Dresselhaus and P. C. Eklund. Phonons in carbon nanotubes. *Advances in Physics*, 49:705–814, 2000.

[23] P. C. Eklund, J. M. Holden, and R. A. Jishi. Vibrational modes of carbon nanotubes spectroscopy and theory. *Carbon*, 33:959–972, 1995.

[24] A. Ferrari and J. Robertson. Resonant Raman spectroscopy of disorderd, amorphous, and diamondlike carbon. *Physical Review B*, 64:075414, 2001.

[25] A. C. Ferrari and J. Robertson. Interpretation of Raman spectra of disorderd and amorphous carbon. *Physical Review B*, 61:14095, 2000.

[26] A. Filho, A. Jorio, and G. G. S. et al. Competing spring constant versus double resonance effects on the properities of dispersive modes in isolated single-wall carbon nanotubes. *Physcial Review B*, 67:035427, 2003.

[27] A. Filho, A. Jorio, J. Hafner, and C. L. etal. Electronic transition energy E_{ii} for an isolated (n,m) single-wall carbon nanotube obtained by anti-Stokes/Stokes resonant Raman intensity ratio. *Physical Review B*, 63:241404, 2001.

[28] B. Gao, L. Jiang, X. Ling, J. Zhang, and Z. Liu. Chirality-dependent raman frequency variation of single-walled carbon nanotubes under uniaxial strain. *Physical Chemical Letters C*, 112:20123, 2008.

[29] Y. Gao, F. Liang, and G. F. et al. Laser sintering of carbon nanotube-reinforced ceramic nanocomposites. *International Journal of Smart and Nano Materials*, iFirst:1–11, 2011.

[30] M. Golabczak and A. Konstantynowicz. Raman spectra evaluation of the carbon layers with Voigt profile. *Journal of Achievements in Materials and Manufacturing Engineering*, 37:270, 2009.

[31] J. Gou. Single-walled nanotube buckypaper and nanocomposite. *Polymer International*, 55:1283–1288, 2006.

[32] V. Hadjiev, G. Warren, L. Sun, D. Davis, D. Lagoudas, and H. Sue. Raman microscopy of residual strains in carbon nanotube/epoxy composites. *Carbon*, 48:1750–1756, 2010.

[33] V. G. Hadjiev, C. A. Mithcell, S. Arepalli, J. Bahr, J. Tour, and R. Krishnamoorti. Thermal mismatch strains in sidewall functionalized carbon nanotube/polystyrene nanocomposites. *Journal of Chemical Physics*, 122:124708, 2005.

[34] F. Huang, K. T. Yue, P. Tan, and S. Z. et. al. Temperature dependence of the Raman spectra of carbon nanotubes. *Journal of Applied Physics*, 84:4022–4024, 1998.

[35] P. Huong, R. Cavagnat, P. Ajayan, and O. Stephan. Temperature-dependent vibrational spectra of carbon nanotubes. *Physical Review B*, 51:10048, 1995.

[36] T. Ida, M. Ando, and H. Toraya. Extended pseudo Voigt function for approximating the Voigt profile. *Journal of Applied Crystallography*, 33:1311–1316, July 2000.

[37] S. Iijima. Helical microtubules of graphitic carbon. *Letters to Nature*, 354:56, 1991.

[38] C. Jiang, K. Kempa, J. Zhao, U. Schlecht, U. Kolb, T. Basche, M. Burghard, and A. Mews. Strong enhancement of the Breit-Wigner-Fano Raman line in carbon nanotube bundlescaused by plasmon band formation. *Physical Review B*, 66:161404, 2002.

[39] A. Jorio, A. G. S. Filho, G. Dresselhaus, M. Dresselhaus, A. K. Swan, M. Unlu, B. B. Goldberg, M. A. Pimenta, J. H. Hafner, C. M. Lieber, and R. Saito. G-band resonant Raman study of 62 isolated single-wall carbon nanotubes. *Physical Review B*, 65:155412, 2002.

[40] A. Jorio, M. A. Pimenta, A. G. S. Filho, R. Saito, G. Dresselhaus, and M. S. Dresselhaus. Characterizing carbon nanotube samples with resonance Raman scattering. *New Journal of Physics*, 5:139, 2003.

[41] A. Jorio, R. Saito, G. Dresselhaus, and M. Dresselhaus. Determination of nanotubes properties by Raman spectroscopy. *Philosophical Transactions: Mathematical, Physical and Engineering Sciences*, 362:2311–2336, 2004.

[42] A. Jorio, R. Saito, J. H. Hafner, C. M. Lieber, M. Hunter, T. McClure, G. Dresselhaus, and M. S. Dresselhaus. Structural (n, m) determination of isolated single-wall carbon nanotubes by resonant Raman scattering. *Physical Review Letters*, 86:1118–1121, 2001.

[43] D. Kahn and J. P. Lu. Vibrational modes of carbon nanotubes and nanoropes. *Physical Review B*, 60:6535–6540, 1999.

[44] A. Kasuya, Y. Sasaki, Y. Saito, K. Tohji, and Y. Nishina. Evidence for size-dependent discrete dispersions in single-wall nanotubes. *Physical Review Letters*, 78:4434–4437, 1997.

[45] H. Kataura, Y. Kumazawa, and Y. Maniwa. Optical properties of single-wall carbon nanotubes. *Synthetic Metals*, 103:2555–2558, 1999.

[46] Y. Kawashima and G. Katagiri. Fundamentals, overtones, and combinations in the Raman spectrum of graphite. *Physical Review B*, 52:10053, 1995.

[47] J. F. Kielkopf. New approximation to the Voigt function with applications to spectral-line profile analysis. *Journal of the Optical Society of America*, 63:987–995, 1973.

[48] S. Lee, J. W. Peng, and C. H. Liu. Probing plasma-induced defect formation and oxidation in carbon nanotubes by Raman disperision spectroscopy. *Carbon*, 47:3488, 2009.

[49] S. W. Lee, G.-H. Jeong, and E. E. B. Campbell. In situ Raman measurements of suspended individual single-walled carbon nanotubes under strain. *Nano Letters*, 7(9):2590–2595, 2007.

[50] J. Lehman, M. Terrones, E. Mansfield, K. Hurst, and V. Meunier. Evaluating the characteristics of multiwall carbon nanotubes. *Carbon*, 49:2581–2602, 2011.

[51] D. Leveque and M. Auvray. Study of carbon-fibre strain in model composites by Raman spectroscopy. *Composites Science and Technology*, 56:749–754, 1996.

[52] H. D. Li, K. T. Yue, Z. L. Lian, Y. Zhan, L. X. Zhou, S. L. Zhang, Z. J. Shi, Z. N. Gu, B. B. Liu, R. S. Yang, H. B. Yang, G. T. Zou, Y. Zhang, and S. Iijima. Temperature dependence of the Raman spectra of single-wall carbon nanotubes. *Applied Physics Letters*, 76(15):2053–2055, 2000.

[53] L. Li, R. Nicholas, C. Chen, R. Darton, and S. Baker. Comparative study of photoluminescence of single-walled carbon nanotubes wrapped with sodium dodecyl sulfate, surfactin and polyvinylpyrrolidone. *Nanotechnology*, 16:S202–S205, 2005.

[54] F. Liang, Y. Tang, J. Gou, H. Gu, and G. Song. Multifunctional nanocomposites with high damping performance for aerospace structures. *Proceedings of the ASME 2009 International Mechanical Engineering Congress and Exposition*, page 12542, 2009.

[55] O. Lourie and H. D. Wagner. Evaluation of Youngs modulus of carbon nanotubes by micro-Raman spectroscopy. *Journal of Materials Research*, 13:2418–2422, 1998.

[56] M. Lucas, X. Zhang, I. Palaci, C. Klinke, E. Tosatti, and E. Riedo. Hindered rolling and friction anisotropy in supported carbon nanotubes. *Nature Materials*, 2529:1–6, 2009.

[57] W. Ma, L. Liu, Z. Zhang, R. Yang, G. Liu, and T. Zhang. High-strength composite fibers realizing true potential of carbon nanotubes in polymer matrix through continuous reticulate architecture and molecular level couplings. *Nano Letters*, 9:2855–2861, 2009.

[58] M. Matthews, M. Pimenta, G. Dresselhaus, M. Dresselhaus, and M. Endo. Origin of dispersive effects of the Raman D band in carbon materials. *Physical Review B*, 59:R6585, 1999.

[59] K. P. Meletov, A. V. Krestinin, J. Arvanitidis, D. Christofilos, and G. A. Kourouklis. Temperature effects in the raman spectra of bundled single-wall carbon nanotubes. *Chemical Physcics Letters*, 477:336–339, 2009.

[60] A. Merlen, N. Bendiab, P. Toulemonde, A. Aouizerat, A. S. Miguel, J. L. Sauvajol, G. Montagnac, and H. C. P. Petit. Resonant Raman spectroscopy of single-wall carbon nanotubes under pressure. *Physical Review B*, 72:035409, 2005.

[61] M. Moniruzzaman and K. I. Winey. Polymer nanocomposites containing carbon nanotubes. *Macromolecules*, 39:5194–5205, 2006.

[62] M. Mu, S. Osswald, Y. Gogotsi, and K. I. Winey. An in situ Raman spectroscopy study of stress transfer between carbon nanotubes and polymer. *Nanotechnology*, 20:335703, 2009.

[63] V. Mussi, C. Biale, S. Visentin, and N. B. et al. Raman analysis and mapping for the determination of COOH groups on oxidized single walled carbon nanotubes. *Carbon*, 48:3391, 2010.

[64] G. M. Nascimento, T. Hou, Y. A. Kim, H. Muramatsu, and T. H. et al. Behavior of the high frequency raman modes of double-wall carbon nanotubes after doping with bromine or iodine vapors. *Carbon*, 49:3585–3596, 2011.

[65] K. T. Nguyen, A. Gaur, and M. Shim. Fano lineshape and phonon softening in single isolated metallic carbon nanotubes. *Physical Review Letters*, 98:145504, 2007.

[66] W. Oliver and G. Pharr. An improved technique for determining hardness and elastic modulus using load and displacment sensing indentation experiments. *Journal of Materials Research*, 7:1564, 1992.

[67] S. Osswald, E. Flahaut, and Y. Gogotsi. In situ Raman spectroscopy study of oxidation of double and single-wall carbon nanotubes. *Chem. Mater.*, 18:1525–1533, 2006.

[68] S. Osswald, M. Havel, and Y. Gogotsi. Monitoring oxidation of multiwalled carbon nanotubes by Raman spectroscopy. *Journal of Raman Spectroscopy Europe*, 38:728, 2007.

[69] Y. Ouyang, L. Cong, L. Chen, Q. Liu, and Y. Fang. Raman study on single-walled carbon nanotubes and multiwalled carbon nanotubes with different laser excitation energies. *Physica E*, 40:2386–2389, 2008.

[70] M. Paillet, P. Poncharal, A. Zahab, J.-L. Sauvajol, J. C. Meyer, and S. Roth. Vanishing of the Breit-Wigner-Fano component in individual single-wall carbon nanotubes. *Physical Review Letters*, 94:237401, 2005.

[71] M. Pimenta, E. Hanlon, A. Marucci, and P. Corio. The anomalous dispersion of the disorderd-induced and the second order Raman bands in carbon nanotubes. *Brazilian Journal of Physics*, 30:423, 2000.

[72] M. A. Pimenta, A. Marucci, S. D. M. Brown, M. J. Matthews, A. M. Rao, P. C. Eklund, R. E. Smalley, G. Dresselhaus, and M. S. Dresselhaus. Resonant Raman effect in single-wall carbon nanotubes. *Journal of Material Research*, 13:2396–2404, 1998.

[73] M. A. Pimenta, A. Marucci, S. A. Empedocles, M. G. Bawendi, E. B. Hanlon, A. M. Rao, P. Eklund, R. E. Smalley, G. Dresselhaus, and M. S. Dresselhaus. Raman modes of metallic carbon nanotubes. *Physical Review B*, 58:R16016–R16019, 1998.

[74] V. N. Popov and P. Lambin. Radius and chirality dependence of the radial breathing mode and the G-band phonon modes of single-walled carbon nanotubes. *Physical Review B*, 73:085407, 2006.

[75] N. Pugno. On the strength of the carbon nanotube-based elevator cable: from nanomechanics to megamechanics. *Journal of Physics, Condensed Matter*, 18:S1971, 2006.

[76] M. Pumera and H. Iwai. Multicomponent metallic impurities and their influence upon the electrochemistry of carbon nanotubes. *J. Phys. Chem. C.*, 113:4401–4405, 2009.

[77] S. Raghavan, P. Imbrie, and W. A. Crossley. The spectral analysis of R lines and vibronic sidebands in the emission spectrum of ruby using genetic algorithms. *Applied Spectroscopy*, 62:759–765, 2008.

[78] A. M. Rao, S. Bandow, E. Richter, and P. C. Eklund. Raman spectroscopy of pristine and doped single wall nanotubes. *Thin Solid Films*, 331:141–147, 1998.

[79] A. M. Rao, E. Richter, S. Bandow, B. Chase, P. C. Eklund, K. A. Williams, S. Fang, K. R. Subbaswamy, M. Menon, A. Thess, R. E. Smalley, G. Dresselhaus, and M. S. Dresselhaus. Diameter-selective Raman scattering from vibrational modes in carbon nanotubes. *Science*, 275:187–197, 1997.

[80] R. Rao, J. Reppert, R. Podila, and X. Z. et al. Double resonance Raman study of disorder in CVD-grown single-walled carbon nanotubes. *Carbon*, 49:1318, 2011.

[81] N. R. Raravikar, P. Keblinski, A. M. Rao, M. S. Dresselhaus, L. S. Schadler, and P. M. Ajayan. Temperature dependence of radial breathing mode Raman frequency of single-walled carbon nanotubes. *Physcal Review*, 66:235424, 2002.

[82] R. Ruoff and D. Lorents. Mehcnaical and thermal properties of carbon nanotubes. *Carbon*, 33:925–930, 1995.

[83] A. Sadeszky, H. Muckenhuber, H. Grothe, R. Niessner, and U. Poschl. Raman microspectroscopy of soot and related carbonaceous materials: Spectral analysis and structural information. *Carbon*, 43:1731–1742, 2005.

[84] N. Sahoo, S. Rana, and J. W. Cho. Polymer nanocomposites based on functionalized carbon nanotubes. *Progress in Polymer Science*, 35:837–867, 2010.

[85] R. Saito, A. Gruneis, G. Samsonidze, V. Brar, G. Dresselhaus, M. D. A. Jorio, L. G. Cancado, C. Fantini, M. Pimenta, and A. Filho. Double resonance Raman spectroscopy of single-wall carbon nanotubes. *New Journal of Physics*, 5:157, 2003.

[86] R. Saito, A. Jorio, A. G. S. Filho, G. Dresselhaus, M. S. Dresselhaus, and M. A. Pimenta. Probing phonon dispersion relations of graphite by double Resonance raman scattering. *Physical Review Letters*, 88:027401, 2002.

[87] C. Salzmann, B. Chu, and G. T. et al. Quantitative assessment of carbon nanotube dispersions by Raman spectroscopy. *Carbon*, 45:907–912, 2007.

[88] D. Sanchez-Portal, E. Artacho, and J. S. et al. *ab initio* structural, elastic, and vibrational properties of carbon nanotubes. *Physical Review B*, 59:12678, 1999.

[89] S. Santangelo, G. Messina, G. Faggio, and M. W. et al. Micro-Raman investigation of vandium-oxide coated tubular carbon nanofibers for gas-sensing applications. *Diamond & Related Materials*, 19:590–594, 2010.

[90] A. Selcuk and A. Atkinson. Analysis of the Cr^{3+} luminescence spectra from thermally grown oxide in thermal barrier coatings. *Materials Science and Engineering A*, A335:147–156, 2002. .pdf ok.

[91] M. Sfeir, T. Beetz, F. Wang, L. Huang, and X. H. et al. Optical spectroscopy of individual single-walled carbon nanotubes of defined chiral structure. *Science*, 312:554, 2006.

[92] T. Shimada, T. Sugai, C. Fantini, and M. S. et al. Origin of the 2450 cm^{-1} Raman bands in HOPG, single wall and double wall carbon nanotubes. *Carbon*, 43:1049–1054, 2005.

[93] N. Soin, S. S. Roy, S. Ray, and J. A. McLaughlin. Excitation energy dependence of Raman bands in multiwalled carbon nanotubes. *Journal of Raman Spectroscopy*, 41:1227–1233, 2010.

[94] M. Souza, A. Jorio, C. Fantini, and B. N. et al. Single- and double-resonance Raman G-band processes in carbon nanotubes. *Physical Review B*, 69:241403(R), 2004.

[95] Z. Spitalsky, D. Tasis, and K. Papagelis. Carbon nanotube- polymer composites chemistry, processing, mechanical and eletrical properties. *Progress in Polymer Science*, 35:357–401, 2010.

[96] J. Talla, D. Zhangand, and M. K. et al. A resonance Raman study of carboxyl induced defects in single-walled carbon nanotubes. *Physica B*, 405:4570–4573, 2010.

[97] P. Tan, C. Y. Hu, J. Dong, W. Shen, and B. Zhang. Polarization properties, high-order Raman spectra, and frequency asymmetry between Stokes and anti-Stokes scattering of Raman modes in a graphite whisker. *Physical Review B*, 64:214301, 2001.

[98] B. K. Tay, D. Sheeja, S. Lau, and X. S. et. al. Time and temperature-dependent changes in the structural properties of tetrahedral amorphous carbon films. *Surface and Coatings Technology*, 130:248–251, 2000.

[99] H. Telg, J. Maultzsch, S. Reich, F. Hennrich, and C. Thomsen. Chirality distribution and transition energies of carbon nanotubes. *Physical Review Letters*, 93:177401, 2004.

[100] P. Thompson, D. Cox, and J. Hastings. Rietveld refinement of Debye Scherrer synchrotron X-ray data from Al_2O_3. *Journal of Applied Crystallography*, 20:79–83, October 1986.

[101] C. Thomsen and S. Reich. Double resonant Raman scattering in graphite. *Physical Review Letters*, 85:5214, 2000.

[102] C. Thomsen, S. Reich, A. R. Goni, and H. J. et. al. Intermolecular interaction in carbon nanotube ropes. *Physica Status Solidi (b)*, 215:435, 1999.

[103] E. T. Thostenson, Z. Ren, and T.-W. Chou. Advances in the science and technology of carbon nanotubes and their composites: a review. *Composites Science and Technology*, 61:1899–1912, 2001.

[104] T. Uchida, M. Tachibana, S. Kurita, and K. Kojima. Temperature dependence of the Breit-Wigner-Fano Raman line in single-wall carbon nanotube bundles. *Chemical Physcics Letters*, 400:341–346, 2004.

[105] A. Vega, J. Z. Kovacs, W. Bauhofer, and K. Schulte. Combined Raman and dieletric spectroscopy on the curing behaviour and stress build up of carbon nanotube-epoxy composites. *Composites Science and Tehnology*, 69:1540–1546, 2009.

[106] J. Vegh. Alternative form for the pseudo-Voigt peak shape. *Review of Scientific Instruments*, 76:056107–1:3, 2005.

[107] C. Velasco-Santos, A. L. Martnez-Hernndez, F. T. Fisher, R. Ruoff, and V. M. Castao. Improvement of thermal and mechanical properties of carbon nanotube composites through chemical functionalization. *Chem. Mater.*, 15:4470–4475, 2003.

[108] U. D. Venkateswaran, A. M. Rao, E. Richter, M. Menon, A. Rinzler, R. E. Smalley, and P. C. Eklund. Probing the single-wall carbon nanotube bundle: Raman scattering under high pressure. *Physical Review B*, 59:10928, 1999.

[109] X. Wang, P. Bradford, W. Liu, and H. Z. et al. Mechanical and eletrical property improvment in CNT-Nylon composites through drawing and stretching. *Composites Science and Technology*, 71:1677–1683, 2011.

[110] Y. Wang, D. C. Alsmeyer, and R. L. McCreery. Raman spectroscopy of carbon materials: Structural basis of observed spectra. *Chem. Mater.*, 2:557–563, 1990.

[111] J. Wasyluk, T. Perova, and D. L. et al. Ultraviolet and visible Raman analysis of thin a-C films grown by filtered cathodic arc deposition. *Diamond & Related Materials*, 19:514–517, 2010.

[112] G. Wertheim, M. Butler, K. West, and D. Buchanan. Determination of the Gaussian and Lorentzian content of experimental line shapes. *Review of Scientific Instruments*, 45:1369–1371, 1974.

[113] M. Wong, M. Paramsothy, and X. X. et al. Physical interactions at carbon nanotube-polymer interface. *Polymer*, 44:7757–7764, 2003.

[114] J. Wood, Q. Zhao, and H. Wagner. Orientation of carbon nantoubes in polymers and its detection by Raman spectroscopy. *Composites: Part A*, 32:391, 2001.

[115] S. Yamauchi and Y. Kurimoto. Raman spectroscopic study on pyrolyzed wood and bark of japanese cedar: temperature dependencies of Raman parameters. *Journal of Wood Science*, 49:235–240, 2003.

[116] R. Young and D. Wiles. Profile shape functions in Rietveld refinements. *Journal of Applied Crystallography*, 15:430–438, 1982.

[117] M. Yu, B. Files, S. Arepalli, and R. Ruoff. Tensile loading of topes of single wall carbon nanotubes and their mechanical properties. *Phys. Rev. Lett.*, 84:5552, 2000.

[118] L. Zhang, V. Liao, and Z. Yu. Raman spectroelectrochemistry of a single-wall carbon nanotube bundle. *Carbon*, 48:2582, 2010.

[119] X. Zhao, Y. Ando, L. Qin, H. Kataura, Y. Maniwa, and R. Saito. Multiple splitting of G-band modes from individual multiwalled carbon nanotubes. *Applied Physics Letters*, 81:2550–2552, 2002.

[120] H. Zhou, C. Qiu, H. Yang, and F. Y. et al. Raman spectra and temperature-dependent Raman scattering of carbon nanoscrolls. *Chemical Physics Letters*, 501:475–479, 2011.

[121] Z. Zhou, L. Ci, L. Song, X. Yan, and D. L. et. al. The intrinsic temperature effect of Raman spectra of double-walled carbon nanotubes. *Chemical Physics Letters*, 396:372–376, 2004.

[122] J. Zhu, J. Kim, H. Peng, J. L. Margrave, V. N. Khabashesku, and E. V. Barrera. Improving the dispersion and integration of single-walled carbon nanotubes in epoxy composites through functionalization. *Nano Letters*, 3:1107–1113, 2003.

[123] G. Zickler, B. Smarsly, N. Gierlinger, H. Peterlik, and O. Paris. A reconsideration of the relationship between the crystallite size L_a of carbons determined by X-ray diffraction and Raman spectroscopy. *Carbon*, 44:3239–3246, 2006.